Project No. 09-801

Tritium Sequestration in Gen IV NGNP Gas Stream via Proton Conducting Ceramic Pumps

Reactor Concepts

Franglin (Frank) Chen,
University of South Carolina

In collaboration with:
University of South Carolina
Savannah River National Laboratory

Michael Patterson, Technical POC
Carl Sink, Federal Technical POC

NEUP Nuclear Energy University Programs
U.S. Department of Energy

NEUP FINAL PROJECT REPORT

Project #: 09-510

Project Report ID: 09-801

Project Tracking ID: CFP-09-801

Project Name: Tritium Sequestration in Gen IV NGNP Gas Stream via Proton Conducting Ceramic Pumps

Performance Period: October 1, 2009 – September 30, 2011

Organization: University of South Carolina

Principal Investigator: Fanglin (Frank) Chen

Collaborators: Thad M. Adams - Savannah River National Laboratory
Kyle Brinkman - Savannah River National Laboratory
Kenneth Reifsnider - University of South Carolina

Table of Contents

1. EXECUTIVE SUMMARY 3
2. APPROACHES AND RESULTS.....5
2.1 Foreword.....5
2.2 Background.....6
2.3 Objectives 7
2.4 Methods 8
2.4.1 Synthesis of Nano-Crystalline Proton Conductor Powders 8
2.4.2 Development of Mixed Protonic and Electronic Conducting Composites 9
2.4.3 Fabrication of Dense Proton-conducting Thin Film 9
2.4.4 Electrochemical Characterization of the High temperature Proton Conductors..... 10
2.5 Results and Key Findings 10
2.5.1 A-site Doping on $BaCe_{0.8}Y_{0.2}O_{3-\delta}$ Simple Perovskite Proton Conductor 10
2.5.2 B-site Y and Yb Co-doping on $BaCe_{0.7}Zr_{0.1}Y_{0.1}Yb_{0.1}O_{3-\delta}$ Proton Conductor 12
2.5.3 Synthesis and Characterization of $BaIn_{0.3-x}Y_xCe_{0.7}O_{3-\delta}$ Proton Conductor..... 14
2.5.4 B-site In and Yb Co-dpoing of $BaCe_{0.7}In_{0.2}Yb_{0.1}O_{3-\delta}$ Proton Conductor..... 19
2.5.5 Layered Perovskite $PrBa_{0.5}Sr_{0.5}Co_2O_{5+\delta}$ as High Performance Catalyst for Proton Conducting Separation Membranes..... 21
2.5.6 Infiltrated Multiscale porous $Sm_{0.5}Sr_{0.5}CoO_{3-\delta}$-$BaZr_{0.1}Ce_{0.7}Y_{0.2}O_{3-\delta}$ Catalyst for Proton-conducting Hydrogen Separation Membranes 25
2.5.7 Fabrication and Characterization of Metal/Ceramic-supported Micro-tubular Hydrogen Separation Membrane Based on $BaCe_{0.7}Zr_{0.1}Y_{0.1}Yb_{0.1}O_{3-\delta}$ 28
2.5.8 Permeation Evaluation of $SrCe0._{095}Yb_{0.05}O_3$ Proton Conducting Ceramic and Thin Films 30
3. CONCLUSIONS.....33
NEUP-09-510 PUBLICATION AND PRESENTATION LIST 34
REFERENCES 36

1. EXECUTIVE SUMMARY

Several perovskite structured proton conductors based on $SrCeO_3$ and $BaCeO_3$ have been investigated in the project. The solid solutions for $SrCeO_3$ and $BaCeO_3$ were first investigated. The morphological and electrical properties of $Ba_{1-x}Sr_xCe_{0.8}Y_{0.2}O_{3-\delta}$ with x varying from 0 to 1 prepared by a modified Pechini method were investigated as potential high temperature proton conductors. Dense microstructures were achieved for all the samples upon sintering at 1500°C for 5 h. The phase structure analysis indicated that perovskite phase was formed for $0 \leq x \leq 0.2$, while for x larger than 0.5, impurity phases of Sr_2CeO_4 and Y_2O_3 appeared. The stability tests indicated that the resistance to boiling water for $Ba_{1-x}Sr_xCe_{0.8}Y_{0.2}O_{3-\delta}$ was between that of $BaCe_{0.8}Y_{0.2}O_{3-\delta}$ and $SrCe_{0.8}Y_{0.2}O_{3-\delta}$. Due to the tendency of the reaction with CO_2 for both $BaCe_{0.8}Y_{0.2}O_{3-\delta}$ and $SrCe_{0.8}Y_{0.2}O_{3-\delta}$, it was not surprising that $Ba_{1-x}Sr_xCe_{0.8}Y_{0.2}O_{3-\delta}$ was also not stable in CO_2 containing atmospheres. The conductivity tests indicated that $Ba_{1-x}Sr_xCe_{0.8}Y_{0.2}O_{3-\delta}$ possessed the electrical conductivity between $BaCe_{0.8}Y_{0.2}O_{3-\delta}$ and $SrCe_{0.8}Y_{0.2}O_{3-\delta}$. The conductivity decreased and the activation energy increased with the increase in Sr content in $Ba_{1-x}Sr_xCe_{0.8}Y_{0.2}O_{3-\delta}$.

The B site co-doping method was then chosen to search novel high temperature proton conductors. Novel proton conductor $BaCe_{0.7}In_{0.2}Yb_{0.1}O_{3-\delta}$ (BCIYb) has been successfully synthesized by a modified Pechini method and characterized as electrolyte for intermediate temperature solid oxide fuel cells. Acceptable tolerance to wet CO_2 environment was found during chemical stability tests. No interaction between the BCIYb membrane and $La_{0.6}Sr_{0.4}Co_{0.2}Fe_{0.8}O_{3-\delta}$ (LSCF) catalyst was observed during the catalyst fabrication process. Further, no detectable impurity phase was found when the BCIYb-LSCF mixed powders were calcined at 700 °C for 50 h. BCIYb dense samples sintered at 1450 °C for 5 h showed acceptable conductivities of 7.2×10^{-3}, 8×10^{-3}, 4.5×10^{-3} and 3.1×10^{-3} Scm^{-1} at 800 °C in dry air, wet air, wet H_2 and wet N_2, respectively. The sinterability of $BaIn_{0.3-x}Y_xCe_{0.7}O_{3-\delta}$ (with x=0-0.3) increased with the increase of In-doping, and the perovskite phase was found in the $BaIn_{0.3-x}Y_xCe_{0.7}O_{3-\delta}$ solid solutions over the range $0 \leq x \leq 0.3$. The conductivities decreased from x=0.3 to 0 while the tolerance to wet CO_2 improved for $BaIn_{0.3-x}Y_xCe_{0.7}O_{3-\delta}$ samples with an increase of In-doping. $BaIn_{0.1}Y_{0.2}Ce_{0.7}O_{3-\delta}$ was found to have relatively high conductivity as well as acceptable wet CO_2 stability.

Zr, Y and Yb co-doped $BaCe_{0.7}Zr_{0.1}Y_{0.1}Yb_{0.1}O_{3-\delta}$ proton conducting material has been prepared by a modified Pechini method. Pure perovskite structured material has been obtained after calcining at temperatures T ≥1000°C. The microstructures of the samples sintered at different temperatures from 1350 to 1550°C have been evaluated, revealing denser microstructures with higher sintering temperatures. The sample sintered at 1400°C shows the highest conductivity, indicating that the beneficial effects on conductivity from denser samples is counteracted by the segregation of secondary phases in the grain boundaries at higher sintering temperatures. The thermal expansion coefficient (TEC) for $BaCe_{0.7}Zr_{0.1}Y_{0.1}Yb_{0.1}O_{3-\delta}$ is in the range of $9.1\text{-}9.8\times10^{-6}$ K^{-1} from 25 to 1200°C.

Layered perovskite structured $PrBa_{0.5}Sr_{0.5}Co_2O_{5+\delta}$ (PBSC) was investigated as a catalytic material for hydrogen separation membrane based on proton conductor $BaCe_{0.7}Zr_{0.1}Y_{0.1}Yb_{0.1}O_{3-\delta}$ (BCZYYb). The sintering conditions for the PBSC-BCZYYb composite were optimized, resulting in the lowest area-specific resistance and apparent activation energy obtained with the

catalyst sintered at 1200°C for 2h. Metal/ceramic-supported micro-tubular proton conducting membranes based on a proton and oxide ion mixed conductor $BaCe_{0.7}Zr_{0.1}Y_{0.1}Yb_{0.1}O_{3-\delta}$ (BCZYYb) have been fabricated using phase inversion and dip-coating techniques with a co-firing process.

Infiltrated multiscale porous catalysts for hydrogen separation membrane have been developed. A $Sm_{0.5}Sr_{0.5}CoO_{3-\delta}$ (SSC)-$BaZr_{0.1}Ce_{0.7}Y_{0.2}O_{3-\delta}$ (BZCY) composite catalyst with multiscale porous structure was successfully fabricated through infiltration for proton-conducting hydrogen separation membranes. The multiscale porous SSC catalyst was coated on the BZCY backbones. Cell polarization resistances were found to be as low as 0.388, 0.162, and 0.064 $\Omega \cdot cm^2$ at 600, 650 and 700 °C, respectively. Compared with the infiltrated multiscale porous catalyst, cells with screen-printed SSC-BZCY composite catalyst showed much higher polarization resistance. This work has demonstrated a promising approach in fabricating high performance proton-conducting separation membranes.

Finally, the isotope effects on permeation for the proton conductor $SrCe0._{095}Yb_{0.05}O_3$ have been investigated. The conductivity of $SrCe0._{095}Yb_{0.05}O_3$ sample in deuterium is lower than the proton conductivity due to the larger mass being transported via hopping through the oxygen sublattice. Tritium conductivity is expected to be correspondingly lower than deuterium necessitating longer times and/or larger membrane area for removal from He gas streams.

2. APPROACHES AND RESULTS

2.1 Foreword

Many studies predict that global oil production is likely to peak within the next 5 to 15 years. With increasing demands for energy, declining global oil reserves and consequent concerns over the supply of liquid fuels for transportation for future generations, increasing pollution and global warming prospects, there is an increasing worldwide interest in the hydrogen (H_2) economy and hydrogen technologies. Gen IV NGNP systems such as the Very High Temperature gas-cooled Reactor (VHTR) can produce hydrogen from only heat and water using sulfur-iodine thermochemical cycle and hybrid sulfur thermochemical process, high temperature electrolysis, or steam reforming of natural gas thus acting as distributed hydrogen generation sites[1]. A distinguishing characteristic of the NGNP from established commercial nuclear plants is the presence of a thermal energy connection between the nuclear plant and a non-nuclear user of high-temperature heat. In the NGNP, thermal energy is delivered from the core of the nuclear reactor to a downstream user without the intermediate conversion of thermal energy into electrical energy, and this is accomplished by heat transfer through heat exchangers and the bulk movement of heat transfer fluids through conduits. This heat can also be used in other thermodynamic power cycles or in industrial processes; with the caveat that the heat supplied by fluids used to cool the reactors is free from radiation contamination before passing from the nuclear plant to the commercial hydrogen/energy/industrial use station. Experiments have shown that trace levels of tritium and tritiated species are typically present at levels less than 1% in the sweep gas for solid breeder reactors.

Tritium, the only radioactive isotope of hydrogen with half-life $t_{1/2}$ of 12.3 years, is relatively similar to hydrogen, which makes it bind to OH as tritiated water (HTO), and it can make organic bonds (OBT) easily. The HTO and the OBT are easily ingested by drinking, through organic or water-containing foodstuffs. Although tritium is not a strong beta emitter, and it is not dangerous externally, it is a radiation hazard when inhaled, ingested via food or water, or absorbed through the skin[2]. Due to the potential health hazard from the ingestion or absorption of tritium, tritium emissions to the environment are regulated by the U.S. Nuclear Regulatory Commission (NRC) and the U.S. Environmental Protection Agency (EPA). Since tritium behaves chemically as hydrogen, it can undergo isotope exchange reactions with hydrogen-containing chemicals (e.g., H_2O, H_2, CH_4, etc.) in downstream industrial processes and become incorporated into the plant's process chemicals or products, but incorporation of tritium in any significant amount may lead to a number of problems. Maintenance of the downstream facilities becomes more complicated because radiation dose to workers becomes a consideration. Also, customers of the downstream facilities may have little to no tolerance for a radioactive product, and so contamination of downstream facilities with tritium may lead to rejected product and loss of revenue for the plant.

There are two principle methods to prevent tritium from reaching the downstream user in any significant amount. The first one is to reduce the tritium permeability of heat exchangers through tritium barrier coating[3]. Although various ceramic coating materials need to be evaluated as potential tritium barrier coatings, it is challenging to find an appropriate coating material satisfying the requirements of permeation reduction factors of 10^3 or greater at the highest temperatures of interest which have self-healing capability if the barrier material is subject to damage from temperature cycling in order to reduce the potential for excess tritium

contamination in the downstream plant[4]. The second method to mitigate tritium contamination is to deploy tritium separation systems on the heat transfer fluid loops in order to remove tritium from those streams, thus making it unavailable to downstream processes. This is a preferred approach since it gives flexibility for utilization of the valuable heat from the NGNP without complication of tritium contamination issues. One effective approach to capture tritium from the nuclear fission gas stream is through tritium getters, materials which can absorb tritium[5]. Metal hydride is widely used for tritium capture, processing and storage in nuclear energy industry and typical the metals used are uranium, titanium and zirconium. In addition, many hydrogen-absorbing alloys such as $LaNi_5$ and FeTi as well as hydrogen-absorbing compounds including ZrNi and $Zr(V_xFe_{1-x})_2$ have been developed as tritium getters for effective utilization of hydrogen energy resources[6]. However, tritium getters typically work at low temperatures, usually less than 500ºC[7]. Therefore, the exhaust hot gas stream from the Gen IV NGNP must be cooled down to lower temperature appropriate for tritium getting and consequently the heat energy available to be captured and utilized in hydrogen production and other industrial processes will be substantially reduced. Another approach for tritium separation and capture is to apply a tritium permeation membrane to filter tritium from the hot gas stream. Precious metals such as Pd and its alloys show good hydrogen permeability[8], however they also show operating temperature limitations and suffer reduced hydrogen permeability from contaminants such as CO, CO_2 and H_2O which are typically present in the gas stream[9].

A potential strategy to overcome the limitation of tritium sequestration in situ from the Gen IV NGNP exhaust gas stream at high temperature is application of a high temperature hydrogen-pump using dense membrane technologies. A composite cermets membrane composed of Pd or other refractory metals and a ceramic material consisting of Al_2O_3, $BaTiO_3$, $SrTiO_3$, ZrO_2, or combinations of them has been recently developed, appropriate for the operating temperature range of 600-1000ºC[10]. However, no data have been reported on the intrinsic permeability of the material and the stability of such membranes. Consequently, a robust hydrogen permeation membrane capable of high temperature operation with good stability is highly appealing and of great significance for in-situ tritium sequestration for the NGNP system. This research project plans to prepare i) conventional hydrogen electrochemical pumps with high temperature proton conducting ceramics, ii) hydrogen permeation membranes with mixed protonic-electronic conducting materials as catalyst made from ceramic/metal and ceramic/ceramic composites, iii) process-microstructure-property relationships for enhanced conductivity and electrode performance, and iv) thin film fabrication of proton conducting ceramics and derivatives on porous ceramic substrates for enhanced hydrogen removal/sequestration rates for further tritium sequestration. This work will bring a new paradigm to in-situ sequestration of tritium from the NGNP cooling stream so that high-temperature heat can be effectively supplied to the downstream users.

2.2 Background

Following the discovery of high temperature proton conduction of the perovskite-type ceramics, dense ceramic membranes have received great attention due to their low cost and high efficiency in hydrogen separation and production[11]. This approach has recently been employed in the fusion community in the ITER project for tritium removal from helium cooled gas streams[12]. In these initial studies, high temperature proton conductors (HTPCs) are used as the electrolytes for electrochemical hydrogen pumps as shown in Fig. 2-1. When an electrochemical cell of a proton

conductor is constructed and a direct current is applied to the cell, hydrogen (and its isotopes) in the anode compartment can be electrochemically pumped to the cathode by the following electrode reactions

$H_2 \rightarrow 2H^+ + 2e^-$ (anode) (2-1)

$2H^+ + 2e^- \rightarrow H_2$ (cathode) (2-2)

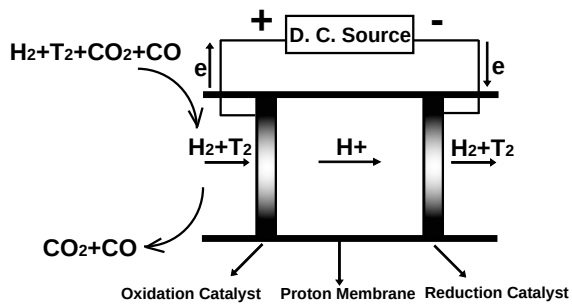

Fig. 2-1 Principle of electrochemical hydrogen pump using proton conducting ceramic.

The hydrogen pumps described above employ the HTPCs as proton-conducting electrolytes that have negligibly low electronic conductivity under operation, thus requiring an externally applied power source to drive the hydrogen separation. The performance characteristics of this process using $CaZrO_3$ based ceramics at 800°C using a permeation surface area of 47cm^2 were reported to be effective for extracting dilute hydrogen from hydrogen/argon mixed gas streams. Gas streams with 0.1% hydrogen were completely separated with hydrogen removal rates of 0.2ml/min at 2.5V applied bias (20mA current)[13]. The driving force for hydrogen (tritium) motion is the external bias applied across the two electrodes on the HTPC membrane and tritium can be extracted from the hot exhaust gas stream and then chemically transformed to tritiated water (HTO) vapor followed by collection and disposal. Enhanced protonic conductivity and thin film membranes are preferred for the hydrogen pump using the HTPC membrane in order to minimize ohmic loss and improve hydrogen permeation rate. In addition, the electrodes are the locations where hydrogen oxidation and reduction take place. If the cathodes can be made hierarchically porous with macro and meso- porosity, the macropores will facilitate mass transport while the mesopores will provide increased reaction sites for electrochemical reaction, and the electrode performance is consequently expected to be greatly enhanced. However, the challenge lies in fabrication of thin film membranes and the creation of a versatile approach to fabricate the hierarchically porous electrodes; that is the focus of this work.

The major concern relates to the availability of suitable proton conductors with high proton conductivity that are stable at the operating temperatures (850-900ºC), and the compatibility with cathode and anode catalysts. It is also known that the microstructure of ceramic materials impacts the levels and mechanism of electronic/ionic conductivity and ultimately the transport/gas separation properties of these materials In addition, the conductivity may be tailored by adding secondary metallic phases, thus forming a “cermet” membrane. Other major challenges that chemical and thermal compatibility exists between different components, and that the fabrication and optimization of the microstructure can provide dense, defect-free thin-film membranes. The proposed work will address the above issues and provide fundamental understanding of the feasibility of tritium sequestration using high temperature protonic conducting materials.

2.3 Objectives

This proposal is aimed at addressing issues related to tritium sequestration for effective utilization of heat in the Gen IV Next Generation Nuclear Plant (NGNP) nuclear power

initiative. A technical hurdle to the use of heat from the high temperature exhaust (with an outlet temperature expected to be 850-900°C) produced in the next generation nuclear processes in commercial applications such as nuclear hydrogen production is the trace levels of tritium present in the exhaust gas streams. This presents a significant challenge since the removal of tritium (usually accomplished at low temperatures through tritium permeable membrane or hydrogen isotope getters) from the high temperature gas stream must be accomplished at elevated temperatures in order to subsequently make use of this heat in downstream processing. The objective of this project is to experimentally evaluate alternative tritium separation technology based on ceramic separation membrane materials with high temperature proton conductivity. The focus will be on the demonstration of the feasibility of tritium sequestration via fabrication and performance evaluation of thin film high temperature nanocrystalline proton conductors, with different microstructure geometries such as thin film and nanocrystalline structures, as well as development of mixed protonic and electronic conducting thin films for high temperature tritium permeation systems.

2.4 Methods

2.4.1 Synthesis of Nano-Crystalline Proton Conductor Powders

The electrical properties of the high temperature perovskite type protonic conducting ceramics are greatly influenced by the crystal structure and microstructure of the material. In general, applications of the ionic conducting materials always start with the synthesis of the corresponding ceramic powders, and the conventional solid state reaction route is often applied. In this method, different kinds of metal oxides and/or carbonates mixed in stoichiometric ratio to yield a given composition are ball-milled, ground and fired at high temperatures. Such a synthesis method often leads to the following disadvantages: (1) a micro-homogenous phase structure is very difficult to obtain due to large and strongly bonded powder agglomerates; (2) contamination can hardly be avoided during milling and grinding, resulting in detrimental effects on the electrical conductivity; and (3) the mechanically ground mixture requires prolonged calcination at high temperatures (usually >1400ºC), which is undesirable in the fabrication of dense fine grained ceramics due to the promotion of abnormal crystallite growth. We have synthesized $SrCeO_3$ and $BaCeO_3$ based high temperature proton conducting powders using a chelating wet-chemistry technique as shown in Fig. 2-2. Compared with the conventional solid-state reaction method to synthesize high temperature protonic conductors, the advantage of a wet-chemistry technique with the help of chelating ligand is that the constituent ions are mixed at the atomic level in the solution so that nano-sized precipitates can be formed by controlling the precipitation parameters such as temperature, solution concentration, nucleation and growth kinetics of the precipitate as well as pH value of the solution.

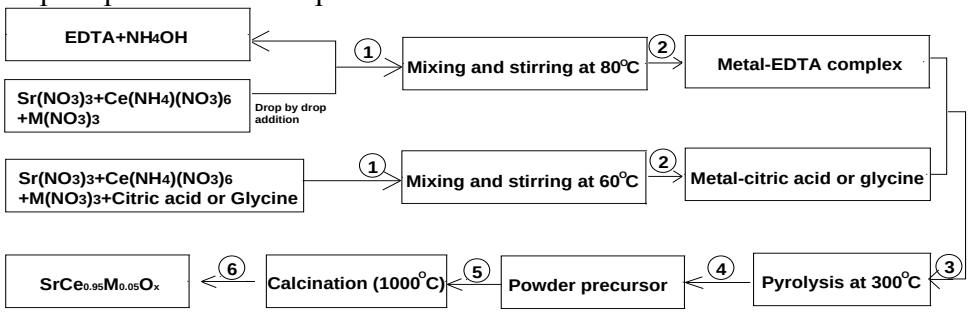

Fig. 2-2 Processing procedure for the preparation of $SrCe_{1-x}M_xO_3$ (x=0.05, M=Yb, or Y) proton conductor powders.

2.4.2 Development of Mixed Protonic and Electronic Conducting Composites

As stated above, a mixed protonic and electronic conducting composite membrane eliminates the need for an external bias in order to extract hydrogen isotopes. The proton conduction through the composite membrane is accomplished by the gradient of hydrogen concentration on the two sides of the membrane. By controlling the sweep gas stream, tritium in the nuclear reactor exhaust stream can be removed. Two types of composite membranes will be studied; the first one is ceramic/metal and the other one is a ceramic/ceramic composite membrane. For the ceramic/metal composite, proton conductors with metals such as Pd, nickel, and alloys will be studied. Chemical compatibility, stability, mechanical strength, and thermal expansion match will be studied. In addition, the protonic and electronic conductivity of the composite membrane will be evaluated.

2.4.3 Fabrication of Dense Proton-conducting Thin Film

a) Dip Coating Strategy

A nano-sized single phase perovskite powder will be sintered into dense ceramic membrane with optimized grain and grain boundary features. The processing parameters will be controlled to obtain the desired crystal and micro-structure to maximize electrical conductivity. Since the permeation rate of tritium will be in reversely proportional to the thickness of the proton conductor membrane, dense thin films of the proton conductor will be fabricated on porous substrate using a dip coating process. Dip-coating of a sol or slurry is a coating technology that has the potential to produce thin (0.1–1μm) and gas-tight (crack-free) ceramic layers on dense substrates. However, it is difficult to prepare gas-tight film on a porous substrate, even by using multiple layer coating processes. Here, we plan to explore the different influential parameters for the synthesis of dense thin hydrogen permeation membranes deposited on porous substrates.

b) Dry-pressing Technology using Powders from a Novel Self-Rising Approach

Dry-pressing technology is an elegant and cost-effective approach to fabricate dense ceramic membranes. However, preparation of thin and dense film is still a challenge for dry-pressing methods. The key to successful preparation of a thin, dense proton-conducting membrane using dry-pressing technique is the fabrication of highly porous or “foam” like proton-conductor powders with extremely low density. Only materials with low density can make it possible to prepare thin films by dry pressing. The films are pressed by means of punches in a hardened metal die. To make a thin proton-conductor film, the loose powder must be uniformly distributed to form a thick layer before pressing, which is very difficult for common commercial powders. The thickness of the loose powder is several hundreds of times that of the dense films. In addition, the thin film thickness should be readily controlled by the amount of powders used. We plan to use a novel self-rising approach to prepare extremely low density proton conductor powders. The self-rising approach was initially applied in the food industry to produce self-rising flour. In fact, the self-rising flour is a mixture of all-purpose flour and a small quantity of the leavening agent, usually the baking powder. During the baking process, the baking powder decomposes as the temperature rises, emitting CO_2 gas and introducing pores into the dough to make it in-situ leaven. Inspired by this strategy, we have tried to identify an appropriate ‘leavening agent’ that can produce macroporous bulk inorganic materials with very low density. This self-rising approach can also produce hierarchically porous oxides which will be applied as the electrode materials for the electrochemical hydrogen pump using high temperature proton conductors.

2.4.4 Electrochemical Characterization of the High temperature Proton Conductors

Electrical conductivity has been evaluated using electrochemical impedance spectroscopy as well as a hydrogen concentration cell to assess the overall electrical conductivity and to separate protonic and electronic conductivity. The samples were painted with porous platinum ink on both sides of the proton conductor membrane and loaded onto an alumina holder with Pt leads. The Electrical conductivity was measured by A.C. impedance method. A.C. impedance responses were collected with the A.C. amplitude of 10mV in the frequency range between 0.01 Hz and 1 MHz using an electrochemical station (Metek, Versa STAT3-400) in different atmospheres. From the intercepts of impedance plots with the real axis, the ohmic resistance of the samples can be determined. The total conductivity is obtained using the following equation: $\sigma=L/(RS)$, where σ is the conductivity in unit of $(\Omega\cdot cm)^{-1}$, L is the sample thickness in unit of cm, R is the ohmic resistance in unit of Ω and S is the Pt electrode area in unit of cm^2. Phase formation and morphologies of samples were determined using a Mini X-ray powder diffractometer and a scanning electron microscope (FEI-200), respectively.

2.5 Results and Key Findings

2.5.1 A-site Doping on $BaCe_{0.8}Y_{0.2}O_{3-\delta}$ Simple Perovskite Proton Conductor

$SrCeO_3$ and $BaCeO_3$ based perovskite materials exhibit considerable proton conduction when doped with trivalent ions. In certain applications however, including the water gas shift reactions with gas phase carbon species present, the cerate perovskite structure is intrinsically unstable up to intermediate temperatures. For example, although Y-doped $BaCeO_3$ possesses the highest level proton conductivity among all perovskite-type high temperature proton conducting oxides studied so far, barium cerates can easily decompose into barium carbonate and/or barium hydroxide, and cerium oxide at elevated temperatures in CO_2 and/or in humid atmospheres. Consequently, recent works have been focused on the development and optimization of the performance of doped cerates in order to enhance their chemical stabilities without remarkably sacrificing their proton conductivities[14].

On the stability issue, many published papers have reported on the effect of doping ions into either B site or A site for the ABO_3 structure. We first aim to fill the knowledge gap and attempts to more completely understand the stability and the electrical properties of $(Ba,Sr)(Ce,Y)O_{3-\delta}$ materials. $Ba_{1-x}Sr_xCe_{0.8}Y_{0.2}O_{3-\delta}$ (BSCY, x=0, 0.1, 0.2, 0.5, 1, denoted as BCY, BSCY1, BSCY2, BSCY5 and SCY, respectively) were prepared, the phase structure and chemical stability were investigated, and the electrical conductivities were evaluated in this work. The reactivity with water was evaluated in both liquid and gas phase conditions.

In this study, the impact of A site doping on the conductivity and stability for $BaCeO_3$ based materials has been investigated. $Ba_{1-x}Sr_xCe_{0.8}Y_{0.2}O_{3-\delta}$ (BSCY, x=0, 0.1, 0.2, 0.5 and 1) powders were prepared by a modified Pechini method. Starting materials $Ba(NO_3)_2$ (Alfa Aesar, 99.95%), $Sr(NO_3)_2$ (Alfa Aesar, 99%), $Ce(NO_3)_3\cdot 6H_2O$ (Alfa Aesar, 99.5%) and $Y(NO_3)_3\cdot 6H_2O$ (Alfa Aesar, 99.9%) were dissolved in deionized water and the nitrate concentration of the metal ions was determined through titration. Ethylenediaminetetraacetic acid (EDTA, Alfa Aesar, 99%) and citric acid (Alfa Aesar, 99%) were used as chelating and complexing agents, to which ammonium hydroxide (Sigma-Aldrich, NH_3 content 28.0 to 30.0%) was added to promote the dissolution of EDTA in deionized water. Stoichiometric amount of the metal precursors were then added into the chelating and complexing agents with citric acid : metal nitrates : EDTA

molar ratio = 1.5 : 1 : 1.2. The solution was stirred at room temperature for 24 h, followed by heat treatment on a hot plate to obtain a brownish gel. The gel was then heated in a microwave oven to assist in foaming. Subsequently, the dried ashes were heat-treated at 600°C for 4 h in air to remove organic residue, followed by calcining at 1100°C for 5 h in air with a heating rate of 3°C min^{-1}. The obtained powders were pulverized with 8 wt% polyvinyl alcohol (PVA) binder and pressed into pellets under 400 MPa. The green pellets were sintered at 1500°C for 5 h in air.

As shown in Fig. 2-3 (b1-b4), all the sintered samples formed dense microstructures, which meet the gas tightness requirement for electrolytes of SOFCs. To evaluate the stability of BSCY in boiling water, sintered pellets with different Sr contents were tested in boiling water for 4h. It can be seen from Fig. 2-3(a) that when treated in boiling water, $SrCe_{0.8}Y_{0.2}O_{3-\delta}$ is chemically more stable than $BaCe_{0.8}Y_{0.2}O_{3-\delta}$. Proton conductivity (shown in Fig. 2-3(c) and (d)) drops while the activation energy increases with the addition of Sr^{2+} ions into the Ba^{2+} sites due to lower proton conductivity for doped $SrCeO_3$ and the formation of secondary phases such as Sr_2CeO_4 and/or Y_2O_3. Considering both the stability and the conductivity testing results, it can be concluded that $Ba_{0.5}Sr_{0.5}Ce_{0.8}Y_{0.2}O_{3-\delta}$ is an optimum composition by balancing the stability and electrical conductivity.

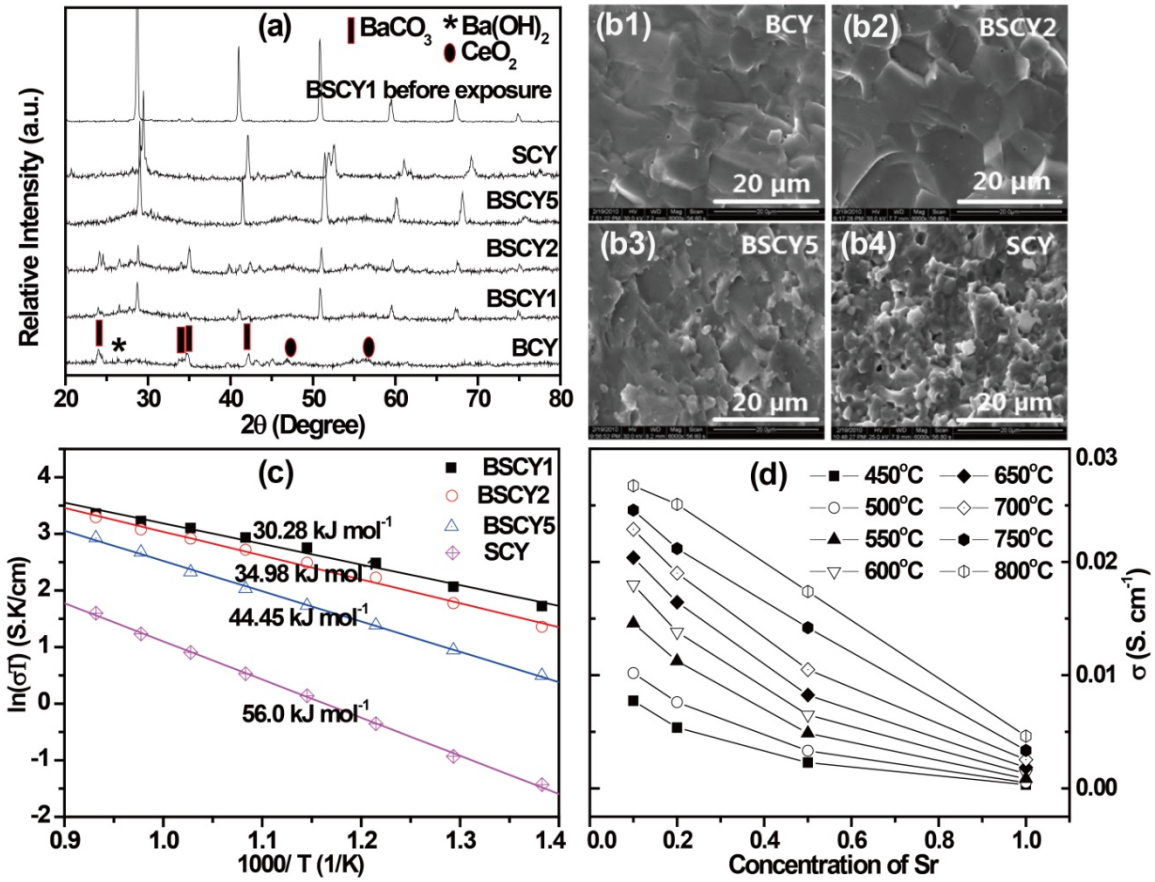

Fig. 2-3 (a) XRD patterns of sintered BSCY pellets (x=0, 0.1, 0.2, 0.5 and 1, denoted as BCY, BSCY1, BSCY2, BSCY5 and SCY, respectively) after exposure in boiling water for 4 h. (b1)-(b4) cross sectional SEM of BSCY electrolyte samples. (c) Arrhenius plots of the electrical

conductivities for BSCY samples in wet H_2 atmosphere. (d) Electrical conductivities for BSCY samples as a function of Sr concentration in wet H_2.

2.5.2 B-site Y and Yb Co-doping on $BaCe_{0.7}Zr_{0.1}Y_{0.1}Yb_{0.1}O_{3-\delta}$ Proton Conductor

Although zirconate-based proton conductors have lower conductivity, they are relatively more stable at elevated temperatures in CO_2 and/or humid atmospheres. To improve the conductivity of the barium zirconate-cerate solid solution, "co-doping" strategy has recently been successfully applied. Barium zirconate and barium cerates containing multiple dopants have been demonstrated to possess higher proton conductivity than the ones containing only a single dopant. It has been recently reported that the conductivity of $BaCe_{0.7}Zr_{0.1}Y_{0.1}Yb_{0.1}O_{3-\delta}$ (BCZYYb) is higher than that of $BaCe_{0.7}Zr_{0.1}Y_{0.2}O_{3-\delta}$ and $BaCe_{0.7}Zr_{0.1}Yb_{0.2}O_{3-\delta}$. Further, BCZYYb shows very promising property for anti-sulfur applications[15]. Consequently, BCZYYb is potentially a promising electrolyte material for SOFC applications. We have prepared $BaCe_{0.7}Zr_{0.1}Y_{0.1}Yb_{0.1}O_{3-\delta}$ by a modified Pechini method and evaluated the sinterability and microstructure evolution of this material. The correlation between the sintering mechanism and the electrical conductivity was also investigated.

Fig. 2-4 (a) shows the XRD patterns of the BCZYYb powders calcined at different temperatures. It can be seen that when the calcination temperature is lower than 800°C, the predominant phases are $BaCO_3$ and CeO_2, with only a small amount of the perovskite phase. Calcination at 900°C results in a perovskite phase dominant structure, with some $BaCO_3$ and CeO_2 impurities. The formation of the $BaCO_3$ impurity is due to the reaction between Ba^{2+} ions and CO_3^{2-} ions which are the product of the reaction between citric acid and/or EDTA and O_2 during heating. When calcined at T $\geq$1000°C, $BaCO_3$ decomposed and a single perovskite phase was obtained. To ensure that all the carbonate impurity was completely decomposed based on the prior studies[16], a calcining process of 1100°C for 5 h has been chosen. Inset in Fig. 2-4 (a) is the SEM of the powder calcined at 1100°C. It reveals a porous morphology with voids distributed inside the powder. Such powder with fluffy morphology has very low filled density and can be used for the fabrication of thin membrane electrolytes using a versatile dry-pressing method, as has been demonstrated previously.

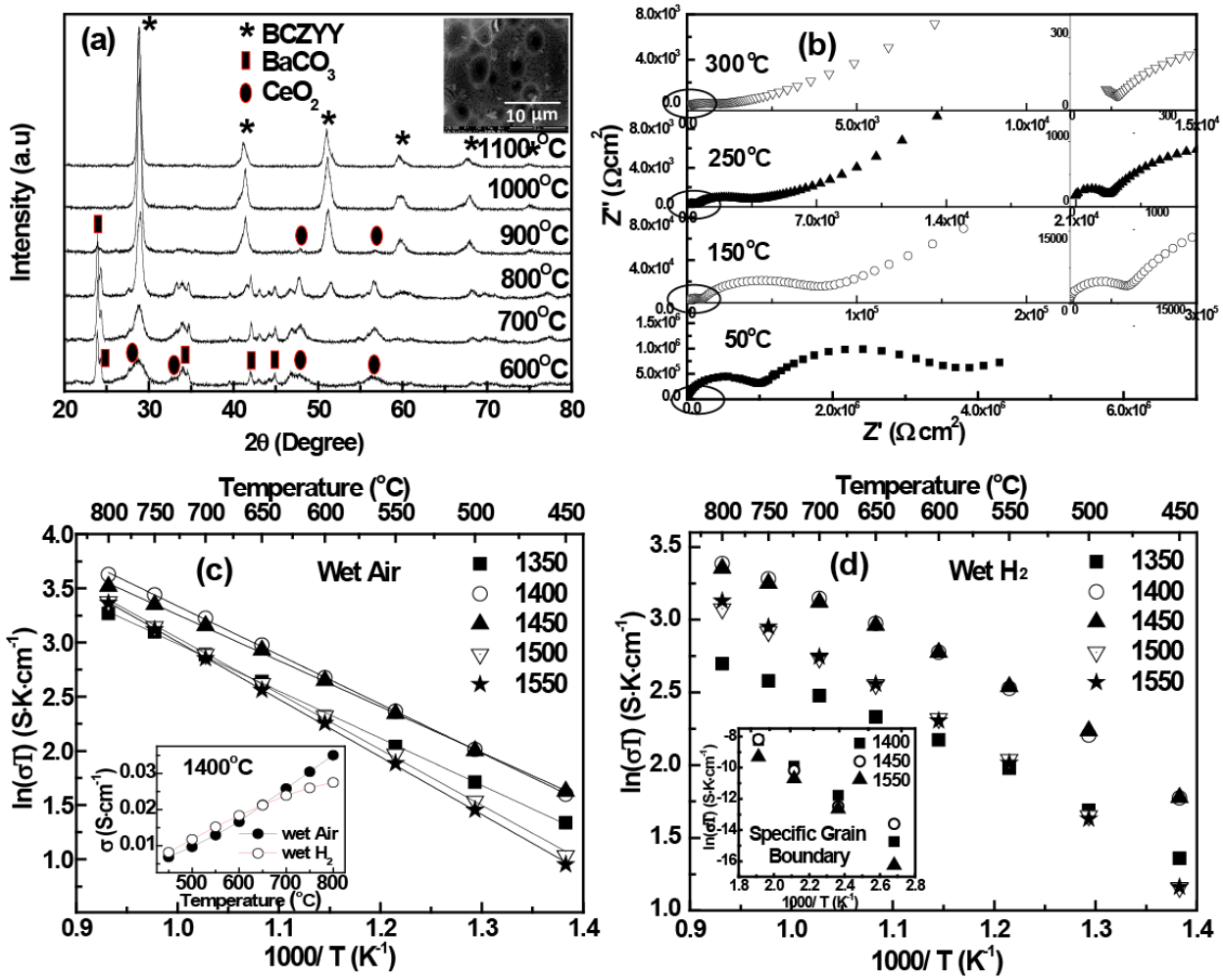

Fig. 2-4 (a) XRD patterns of $BaCe_{0.7}Zr_{0.1}Y_{0.1}Yb_{0.1}O_{3-\delta}$ powder calcined at different temperatures. Inset is the SEM of the powder calcined at 1100°C. (b) Nyquist plots of sample sintered at 1400°C in wet air. Inset pictures are expanded views of the high frequency regions. (c-d) Arrhenius plots of conductivity for BCZYYb samples. Inset in (c) is the conductivity measured in wet air and wet H_2 of the samples sintered at 1400°C; inset in (d) is the specific grain boundary conductivity for BCZYYb sintered samples in wet air.

To further investigate the effect of the sintering temperature on the grain boundary conductivity, the impedance measurements are extended to lower temperatures where the grain boundary contribution can be readily recognized. Fig. 2-4(b) shows the typical Nyquist plots of sample 1400 measured at low temperature range in wet air. The inset pictures are expanded views of high frequency regions for the corresponding impedance spectra. The impedance spectra typically have three semi-circles corresponding to the bulk, grain boundary and electrode responses from high to low frequencies. With an increase in the testing temperature, the semi-circle corresponding to the bulk conduction response gradually disappears. The bulk resistance is then derived from the high frequency intercept of the intermediate arc with the real axis. When the testing temperature was further increased, it became difficult to derive the bulk conduction from grain boundary conduction and only the total conductivity is recorded.

The conductivity tests were conducted on the samples sintered at different temperatures. Fig. 2-4 (c) and (d) show the Arrhenius plots of the conductivities as a function of testing temperature for BCZYYb samples in wet air and wet H_2, respectively. Among the different samples tested in this work, sample 1400 shows the highest conductivity while sample 1550 shows the lowest conductivity. For samples sintered at lower temperatures, the existence of pores and pinholes as can be seen which can result in a reduction in the conductivity. While for the samples sintered at 1500°C and higher, segregation of secondary phases in the grain boundary areas deteriorates the conductivity, consistent with the reported conductivity results for $BaCe_{0.45}Zr_{0.45}Y_{0.1}O_{3-\delta}$, indicating that an optimum sintering temperature exists to obtain the maximum conductivity value as a result of achieving optimum values of density, grain size and phase purity. The activation energies measured in wet air are 36, 38, 35, 43 and 44 kJ mol^{-1} for sample 1350, 1400, 1450, 1500 and 1550, respectively, which are favorably close to the reported values[17]. In wet H_2 atmosphere (Fig. 2-4 (d)), there is a clear tendency of decrease in the activation energy with the increase in testing temperature, reflecting the temperature dependence on proton concentration. The proton concentration in BCZYYb would decrease with an increase in temperature, caused by the dehydration of the materials due to the exothermic nature of the reaction in Equation (2-3) using Kröge-Vink notation[18]

$$H_2O_{(g)} + O_O^{\times} + V_O^{\bullet\bullet} = 2OH_O^{\bullet} \qquad (2\text{-}3)$$

The bowed shapes for the conductivity curves can also be found in other proton conducting materials such as $BaZr_{0.1}Ce_{0.7}Y_{0.2}O_{3-\delta}$ and $BaZr_{0.9}Y_{0.1}O_{3-\delta}$[19]. It is noted that enhancement of conductivity in wet H_2 for the samples tested at reduced temperatures (below 600°C) is observed, indicative of higher proton mobility leading to significant enhancement of proton conductivity at reduced temperatures[20]. As an example, for the sample sintered at 1400°C shown in the inset in Fig. 2-4(c), the conductivity at 550°C increased from 0.013 S cm^{-1} in wet air to 0.015 S cm^{-1} in wet H_2. The conductivity values are comparable to those reported for $BaZr_{0.1}Ce_{0.7}Y_{0.1}Yb_{0.1}O_{3-\delta}$ (about 0.018 S cm^{-1} in wet oxygen at 550°C) and $BaZr_{0.1}Ce_{0.7}Y_{0.2}O_{3-\delta}$ (about 0.01 S cm^{-1} in wet 4% H_2 at 550°C). Since the conductivity data were measured in different atmospheres, a slight deviation can be expected. From the results shown above we can conclude that an optimum sintering temperature of 1400°C has been obtained, resulting in a compromise between densification of samples which will improve the conductivity, and segregation of secondary phases which will deteriorate the conductivity when sintered at high temperatures.

2.5.3 Synthesis and Characterization of $BaIn_{0.3-x}Y_xCe_{0.7}O_{3-\delta}$ Proton Conductor

$BaCeO_3$ and $BaZrO_3$ can easily form a solid solution across the entire composition range. Consequently, it might be possible to replace a fraction of Ce in $BaCeO_3$ with Zr, thereby achieving a solid solution of cerate and zirconate with both good protonic conductivity and chemical stability. Further it has been recently reported that a Zr-free barium cerate (i.e. In-doped $BaCeO_3$) possesses good stability at elevated temperatures in CO_2 and H_2O-rich environments[21]. However, the electrical conductivity of In-doped $BaCeO_3$ proton conductors is relatively low[22]. To improve the conductivity of In-doped $BaCeO_3$ proton conductor, yttria could be used as co-dopant since yttria doped $BaCeO_3$ has high conductivity among doped $BaCeO_3$. The same strategy of "co-doping" has been successfully applied on $BaCe_{0.8-x}M_xY_{0.2}O_{3-\delta}$ with M (M=Ta, Ti, and Sn) and Y as the co-dopants and proved to maintain both high conductivity and good stability[23]. Consequently, it is anticipated that co-doping the B-site with In and Y while maintaining high Ce content (e.g., 0.7) might offer a unique composition with elevated proton conductivity and improved stability in CO_2 and H_2O-rich environments.

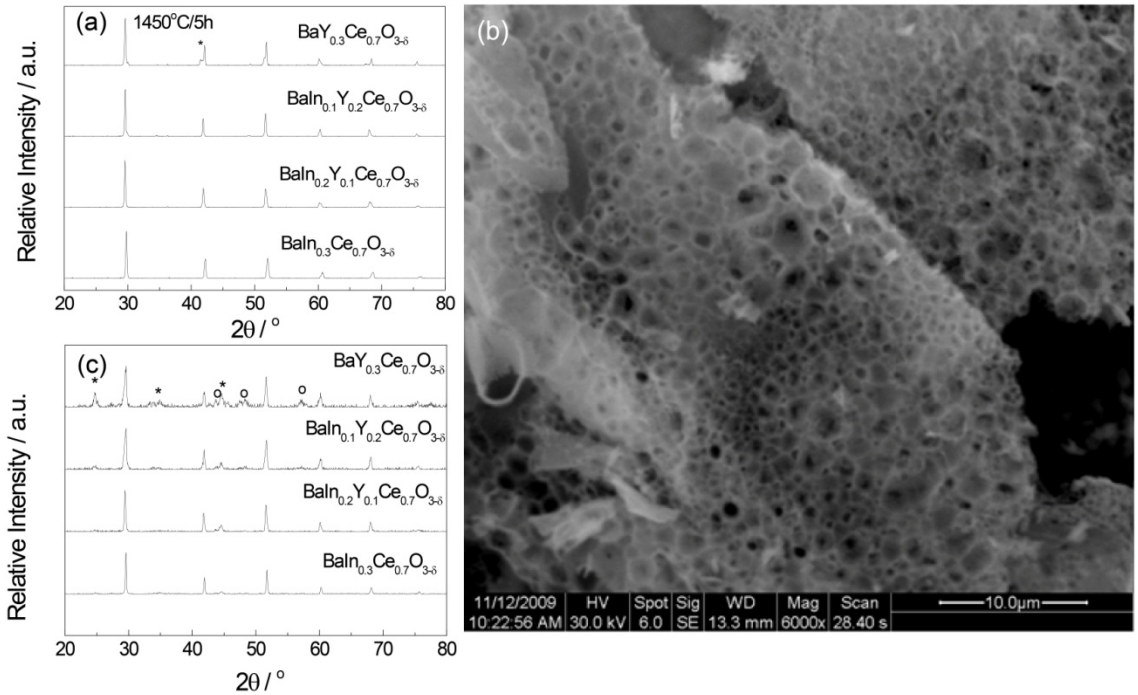

Fig. 2-5 (a) XRD patterns of $BaIn_{0.3-x}Y_xCe_{0.7}O_{3-\delta}$ (x=0, 0.1, 0.2, 0.3) powders sintered at 1450°C for 5h in air. *: Y_2O_3.(b) SEM photograph of $BaIn_{0.3}Ce_{0.7}O_{3-\delta}$ powder sintered at 1000°C for 6h in air.(c) XRD patterns of $BaIn_{0.3-x}Y_xCe_{0.7}O_{3-\delta}$ (x=0, 0.1, 0.2, 0.3) disks measured on the surfaces after exposure to wet 3% CO_2 with air as the balance gas at 700°C for 24h. *: $BaCO_3$, o: CeO_2.

Fig. 2-5 (a) shows the XRD data for $BaIn_{0.3-x}Y_xCe_{0.7}O_{3-\delta}$ as a function of the Y content. A single phase perovskite structure was obtained for most of these compositions. For the In-doped materials, $BaIn_{0.3}Ce_{0.7}O_{3-\delta}$ was determined to be an orthorhombic *Pmcn* unit cell even when the In^{+3} content was increased up to 30%, as reported by Giannici[24]. However, for the Y-doped barium cerate, the Y dopant solubility limit is less than 20% of the available Ce sites. Consequently, the Y_2O_3 phase segregated at the grain boundaries in $BaY_{0.3}Ce_{0.7}O_{3-\delta}$, as can be seen from the XRD pattern in Fig. 2-5 (a). In^{3+} and Y^{3+} have effective ionic radii of 0.80 Å and 0.90 Å, respectively, implying that the doping of Y^{3+} should lead to an increase in lattice parameters. This was confirmed by the XRD peaks for the samples where higher Y-doping resulted in slight peak shift toward lower 2θ, indicating an increase in the lattice parameter. In addition, it was observed that Y^{3+} adapts poorly to insertion in the host lattices in cerate due to its very high hardness. On the other hand, In^{3+}, being much softer than Y^{3+} (i.e., more easily polarized), can be more effectively inserted in the host lattices since its low hardness allows for the release of the resulting strain and consequently stabilizes the structure.

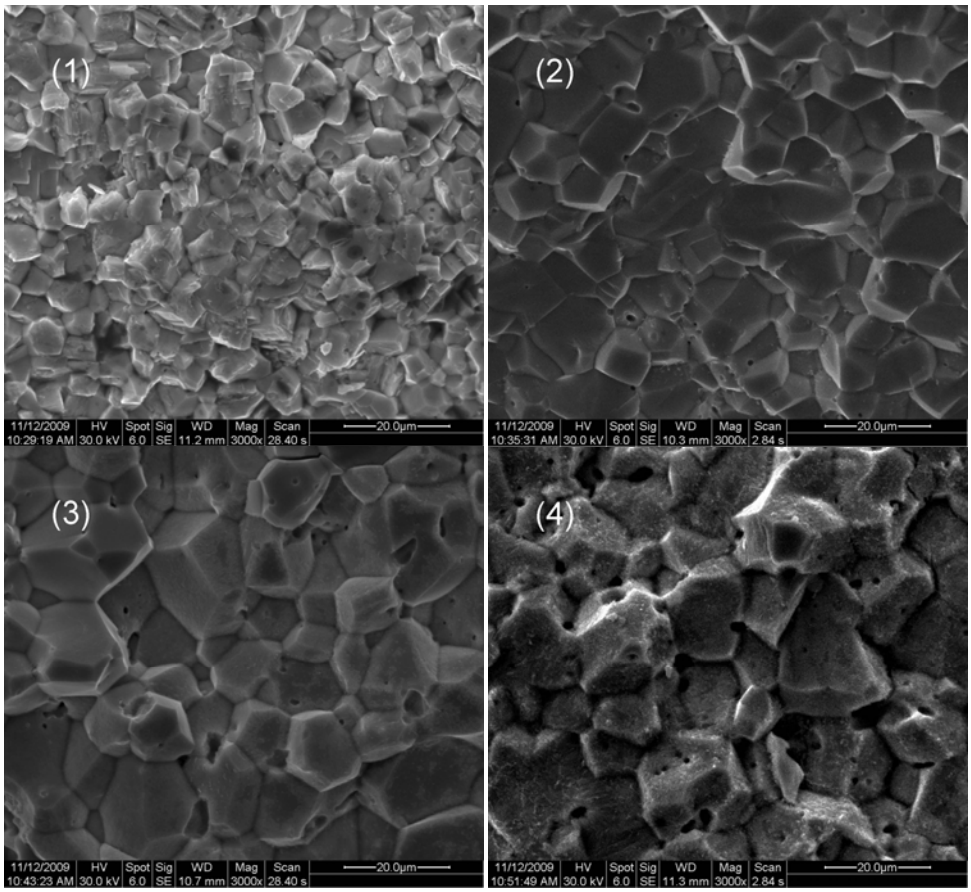

Fig. 2-6 The cross-sectional views of different pellets sintered at 1450°C for 5h in air after all conductivity measurements. (1) $BaIn_{0.3}Ce_{0.7}O_{3-\delta}$ (2) $BaIn_{0.2}Y_{0.1}Ce_{0.7}O_{3-\delta}$ (3) $BaIn_{0.1}Y_{0.2}Ce_{0.7}O_{3-\delta}$ (4) $BaY_{0.3}Ce_{0.7}O_{3-\delta}$.

To investigate the sinterability of the In-doped powders, morphologies of the powders and sintered ceramics were analyzed by SEM. As shown in Fig. 2-5 (b), the SEM image of the $BaIn_{0.3}Ce_{0.7}O_{3-\delta}$ powder calcined at 1000°C for 6 h in air reveals a network-like morphology with plenty of voids distributed inside a foam-like structure. The morphologies for the other BICY powders with different compositions are similar. Such fluffy powders having very low filled density are particularly suitable for fabricating thin membranes by a dry-pressing method[25]. After sintering the BICY pellets at 1450°C for 5h, the size of crystalline grains and the number of closed pores increase with Y doping content as shown from the cross-sectional views of those ceramic disks in Fig. 2-4. The average grain size is determined using a linear intercept method by counting the adjacent grains in the SEM graphs. The average grain sizes are 5.6, 8.5, 12.7 and 15.2µm for $BaIn_{0.3-x}Y_xCe_{0.7}O_{3-\delta}$ (x=0, 0.1, 0.2, 0.3) samples, respectively. The sintering conditions used in this work are normally employed in fabricating $BaCeO_3$-based SOFCs. Of course, from the results in this study it may be expected that high densities of the BIYC samples might be achieved at relatively lower sintering temperature or for shorter dwell time. Further work is needed in order to study when and how the grain growth happens and what the effects of the grain size on chemical stability and conductivity of the sintered BIYC samples. The packing between $BaIn_{0.3}Ce_{0.7}O_{3-\delta}$ crystallites is more compact than that of $BaY_{0.3}CeO_{3-\delta}$, which is

consistent with the shrinkage results of those sintered pellets. After sintering at 1450°C for 5h, the linear shrinkages of the disk diameters are 12.3%, 12.0%, 11.5% and 10.3% for $BaIn_{0.3-x}Y_xCe_{0.7}O_{3-\delta}$ (x=0, 0.1, 0.2, 0.3) samples, respectively. The results of Archimedes's water displacement measurements on the sintered disks showed that all the BIYC sintered samples have relative densities greater than 94% of the theoretic values (e.g. $BaIn_{0.2}Y_{0.1}Ce_{0.7}O_{3-\delta}$ has a theoretical density of 7.165g/cm^3). Consequently, In-doping results in an improved sinterability of BIYC.

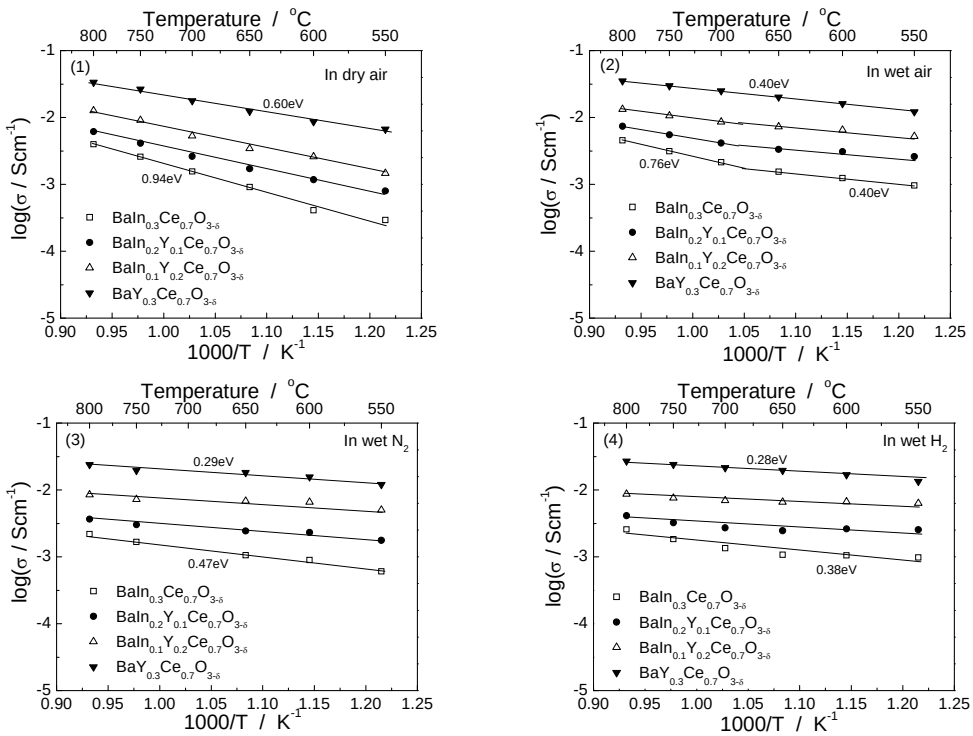

Fig. 2-7 Effect of temperature on the conductivity of the $BaIn_{0.3-x}Y_xCe_{0.7}O_{3-\delta}$ (x=0, 0.1, 0.2, 0.3) samples in dry air (1), wet air (2), wet nitrogen (3) and wet hydrogen (4).

To investigate the chemical stability of the $BaIn_{0.3-x}Y_xCe_{0.7}O_{3-\delta}$ (x=0, 0.1, 0.2, 0.3), the BICY disks were exposed to wet 3vol% CO_2 (air as the balance gas, 3vol% H_2O) with a flow rate of 40 mLmin^{-1} at 700°C for 24 h. The formation of $BaCO_3$ and CeO_2 can be observed in the XRD patterns shown in Fig. 2-5 (c). The number and intensity of the impurity peaks were observed to increase with the increase in Y doping content, suggesting that the tolerance to CO_2 decreases with Y doping for $BaIn_{0.3-x}Y_xCe_{0.7}O_{3-\delta}$ (x=0, 0.1, 0.2, 0.3) ceramics. For example, although the main perovskite structure phase of BICY remains, the reaction between $BaY_{0.3}Ce_{0.7}O_{3-\delta}$ and wet CO_2 is more severe than that for $BaIn_{0.3}Ce_{0.7}O_{3-\delta}$. The intensity of the impurity peaks in the XRD patterns of $BaIn_{0.3}Ce_{0.7}O_{3-\delta}$ is negligible compared to that of the characteristic perovskite peaks, which is consistent with the results reported by Bi et al[21].

Shown in Fig. 2-7 are the conductivities of the $BaIn_{0.3-x}Y_xCe_{0.7}O_{3-\delta}$ (x=0, 0.1, 0.2, 0.3) samples in different atmospheres in the temperature range of 550-800°C. Among all the samples examined, $BaY_{0.3}Ce_{0.7}O_{3-\delta}$ shows the highest conductivities: 3.36×10^{-2}, 3.5×10^{-2}, 2.40×10^{-2} and 2.71×10^{-2} Scm^{-1} in dry air, wet air, wet nitrogen and wet hydrogen at 800°C, respectively. However, the

chemical stability of $BaY_{0.3}Ce_{0.7}O_{3-\delta}$ is quite unsatisfactory according to XRD study shown above. $BaIn_{0.1}Y_{0.2}Ce_{0.7}O_{3-\delta}$ shows an acceptable stability and relatively high conductivity: 1.27×10^{-2}, 1.33×10^{-2}, 8.52×10^{-3} and 8.7×10^{-3} Scm^{-1} in dry air, wet air, wet nitrogen and wet hydrogen at 800°C, respectively. At a given operating temperature, the conductivities of BICY samples increase with the amount of Y doping. This result can be partially predicted by the SEM observations shown in Fig. 2-6 due to the increasing number of grain boundaries in low concentration of the Y–doping. From the change of slope coefficient shown in Fig. 2-7(1), (3) and (4), it indicates that the activation energies for total conductivity of the $BaIn_{0.3-x}Y_xCe_{0.7}O_{3-\delta}$ system in dry air, wet N_2 and wet H_2 decrease with the increase of the Y content. The conductivities of all samples in wet hydrogen (Fig. 2-7(4)) are found to be lower than those in dry (Fig. 2-7(1)) and wet (Fig. 2-7(2)) air, probably due to the presence of oxygen-ion and hole conductivity in air since the hole conductivity depends on the oxygen vacancy concentration introduced through doping with trivalent ions and oxygen partial pressure of the testing environment[26]. Meanwhile, slope changes in Fig. 2-7(2) for the In-doped samples in the temperature regions of 650-700°C could be related to a change of the conduction mechanism when water vapor and air are present, as derived from the change of the effective charge carriers' concentration[27]. As shown in Fig. 2-7(2), the activation energy of $BaIn_{0.3}Ce_{0.7}O_{3-\delta}$ under wet air increased from 0.40eV to 0.76eV, indicating that the predominant conduction phenomena changed from proton conduction at low temperatures to oxygen-ion conduction at high temperatures.

For further H_2 separation measurement, the proton conducting membrane was pasted with catalysts to improve the performance. Ceramic/metal composite catalytic layer was fabricated aiming to enhance the hydrogen separation performance. 65wt.% NiO (J.T. Baker) and 35 wt.% BCIY were prepared by mixing and grinding with an agate mortar and pestle. The powders were first pressed as a substrate. BCIY powder was then added onto the substrate and co-pressed at 300 MPa for 3 min to form a bi-layer, followed by co-sintering at 1450°C for 5 h to form a NiO-BCIY substrate and BCIY proton conducting dense membrane. The thicknesses for the dense BCIY electrolyte membrane were ~45 μm. The NiO-BCIY substrate was then treated in hydrogen atmosphere to be reduced to Ni-BCIY metal/ceramic substrate. It was noticed that the substrates was well bounded to the electrolyte membranes and there were no cracks in the membranes as shown in Fig. 2-8[28].

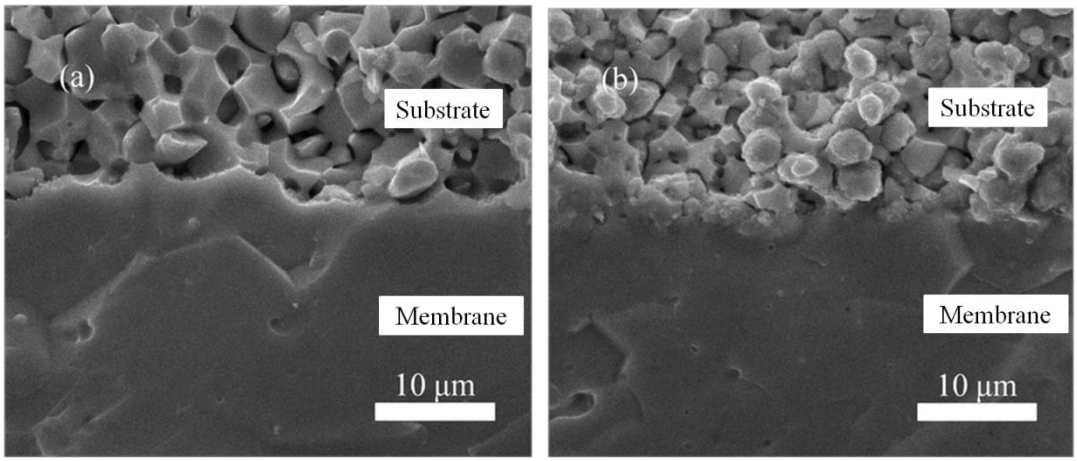

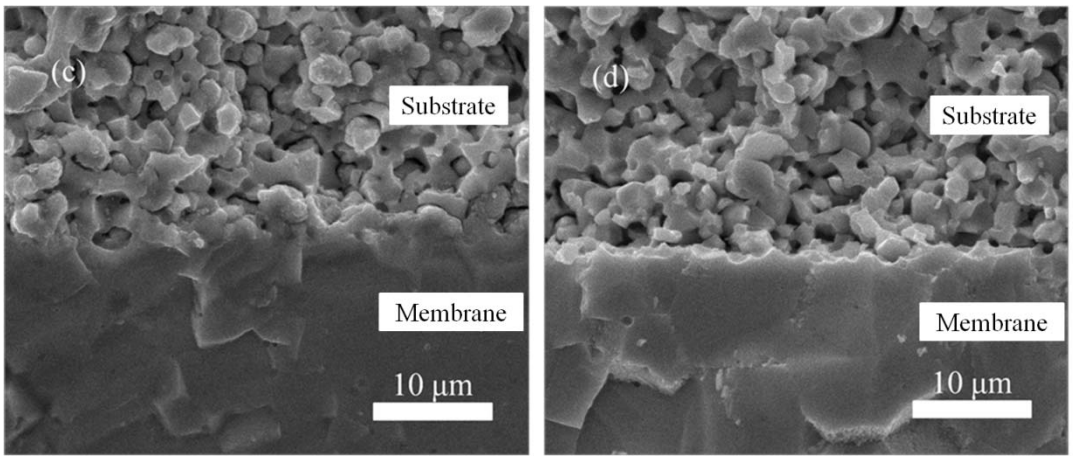

Fig.2-8 Fracture views of substrate/membrane interfaces based on: (a) $BaCe_{0.7}In_{0.3}O_{3-\delta}$, (b) $BaCe_{0.7}In_{0.2}Y_{0.1}O_{3-\delta}$, (c) $BaCe_{0.7}In_{0.1}Y_{0.2}O_{3-\delta}$, and (d) $BaCe_{0.7}Y_{0.3}O_{3-\delta}$.

2.5.4 B-site In and Yb Co-dpoing of $BaCe_{0.7}In_{0.2}Yb_{0.1}O_{3-\delta}$ Proton Conductor

Phase formation and chemical reaction of BCIYb samples were investigated using power XRD study with results shown in Fig. 2-9. Since In^{3+} (0.8 Å) and Yb^{3+} (0.868 Å) have similar ionic radii to that of Ce^{4+} (0.87 Å), a solid solution is expected to form by doping In and Yb in Ce sites. Single phase perovskite structure was confirmed by XRD analysis for the BCIYb pellet sample sintered at 1450 ^{o}C for 5 h in air as shown in Fig. 2-9(a). When the sample was exposed to environmental air at room temperature for 2 months, no impurity peaks were found as shown in Fig. 2-9(b).

For the Yb-doped $BaCeO_3$ sample, XRD diffraction peaks related to $BaCeO_3$ and CeO_2 were reported by Osman et al. after the sintered sample was exposed to CO_2-containing atmosphere[29]. To investigate its tolerance to wet CO_2, the sintered BCIYb sample was heat-treated at 700 ^{o}C for 24 h by introducing a mixed gas consisting 3% H_2O, 3% CO_2 and air (balance gas). No impurity XRD diffraction peaks were detectable, as shown in Fig. 2-9(c), indicating that BCIYb has satisfactory tolerance to wet CO_2. The stability of Yb-doped $BaCeO_3$ is thus significantly improved by Indium co-doping, consistent with the results of In-doped $BaCeO_3$ proton-conducting materials showing good chemical stability. The chemical compatibility between BCIYb powder and commercial LSCF powder has also been investigated in this work. Compared Fig. 2-9(e) with Fig. 2-9(a) and (d), no impurity was observed for BCIYb-LSCF catalytic layer calcined at 1100 ^{o}C for 2 h during the catalytic layer fabrication process. Further, after firing the mixed powders of BCIYb and LSCF at 700 ^{o}C for 50 h in air, no apparent secondary peaks have been observed, indicating that BCIYb electrolyte and LSCF catalytic material are chemically compatible.

Table 2-1. Comparison of total conductivity for doped $BaCeO_3$ in wet H_2

Sample	Total conductivity (Scm^{-1})	
	600 °C	800 °C
$BaCe_{0.9}In_{0.1}O_{3-\delta}$[22]	1.8×10^{-3}	3.4×10^{-3}
$BaCe_{0.9}Yb_{0.1}O_{3-\delta}$[28]	1.5×10^{-2}	3.4×10^{-2}
$BaCe_{0.7}In_{0.2}Yb_{0.1}O_{3-\delta}$ this work	2.7×10^{-3}	4.5×10^{-3}
$BaCe_{0.7}In_{0.2}Y_{0.1}O_{3-\delta}$[21]	2.6×10^{-3}	4.1×10^{-3}
$BaZr_{0.1}Ce_{0.8}Y_{0.1}O_{3-\delta}$[30]	1×10^{-2}	1.5×10^{-2}

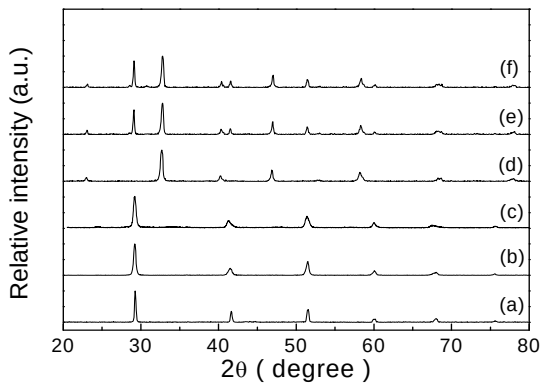

Fig. 2-9 X-ray diffraction patterns for (a) BCIYb pellet sample sintered at 1450 °C for 5 h in air, (b) BCIYb sample after exposure to environmental air at room temperature for 2 months, (c) BCIYb sample after exposure to wet CO_2 (3% H_2O, 3 % CO_2 and air as the balance gas) at 700 °C for 24 h, (d) commercial LSCF, (e) BCIYb-LSCF catalyst calcined at 1100 °C for 2 h in air, and (f) BCIYb-LSCF composite sintered at 700 °C for 50 h in air.

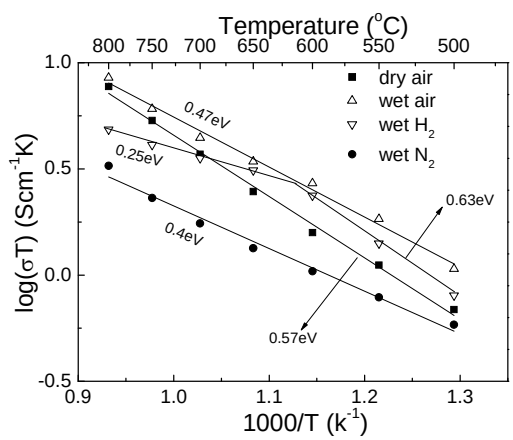

Fig. 2-10 Arrhenius plot of conductivity of BCIYb in different atmospheres in the temperature range of 500-800 °C.

Shown in Fig. 2-10 are the conductivities of the BCIYb sample measured in different atmospheres in the temperature range of 500-800°C. Among all the examined atmospheres,

BCIYb shows the highest conductivity of 8×10^{-3} Scm^{-1} at 800 ^{o}C in wet air, followed by 7×10^{-3}, 4.5×10^{-3} and 3×10^{-3} Scm^{-1} in dry air, wet hydrogen and wet nitrogen, respectively. The conductivities of BCIYb are a little bit higher than those of $BaCe_{0.7}In_{0.2}Y_{0.1}O_{3-\delta}$, which are 7×10^{-3} and 4×10^{-3} Scm^{-1} at 800 ^{o}C in wet air and wet hydrogen, respectively[30]. As shown in Table 2-1, the conductivity of BCIYb falls between $BaCe_{0.9}In_{0.1}O_{3-\delta}$ and $BaCe_{0.9}Yb_{0.1}O_{3-\delta}$, which are 3.4×10^{-3} and 3.4×10^{-2} Scm^{-1} at 800 ^{o}C in wet hydrogen as reported by Matsumoto et al[36]. According to the slope of the Arrhenius plots shown in Fig. 2-10, the activation energies for total conductivity of the BCIYb sample were 0.4, 0.47 and 0.57 eV in wet N_2, wet air and dry air, respectively. However, slope change in wet H_2 was found in Fig. 2-10, showing an activation energy of 0.63 eV at temperatures below 600 ^{o}C and 0.25 eV above 600 ^{o}C, which could be related to a change of effective charge carriers' concentration.

2.5.5 Layered Perovskite $PrBa_{0.5}Sr_{0.5}Co_2O_{5+\delta}$ as High Performance Catalyst for Proton Conducting Separation Membranes

The development of proper catalytic materials for protonic ceramic membranes in order to improve materials compatibility and reduce costs remains a challenge. Noble metals (Pt, Pd) as well as simple perovskite-type mixed ionic–electronic conductors (MIEC) such as $La_{0.6}Sr_{0.4}CoO_{3-\delta}$, $Sm_{0.5}Sr_{0.5}CoO_{3-\delta}$, $La_{0.5}Sr_{0.5}FeO_{3-\delta}$ and $Ba_{0.5}Sr_{0.5}Co_{0.8}Fe_{0.2}O_{3-\delta}$ have been extensively studied as cathodes for solid oxide fuel cells[31]. However, not much attention has been paid to layered perovskite materials. Recently, cation-ordered $LnBaCo_2O_{5+\delta}$ (Ln=La, Pr, Nd, Sm, Gd, and Y) have been systemically investigated as cathodes for oxygen-ion conductor SOFCs[32]. Among the various layered $LnBaCo_2O_{5+\delta}$ oxides, $PrBaCo_2O_{5+\delta}$ has the highest bulk diffusion coefficient, surface exchange coefficient and the lowest area specific polarization resistance for SOFCs based on samarium-doped ceria electrolyte. These results indicate that layer-structured oxides are promising alternative materials for SOFC cathode[33]. Herein we investigate the $PrBaCo_2O_{5+\delta}$ (PBSC) as catalyst materials for proton conducting separation membranes. In this work, the electrochemical performance of the PBSC–BZCY composite catalyst was evaluated using symmetrical cells. In addition, a suspension-coating technique was employed to fabricate the BZCY thin film with PBSC-BZCY composite catalytic layer was also investigated at a range of temperatures.

XRD results of pure PBSC, BZCY powder and PBSC-BZCY composites are shown in Fig. 2-11. The PBSC and BZCY oxides prepared by the modified EDTA-citrate combustion method after calcination at 1100°C for 6h in air are all identified as single phases. In the XRD result presented in Fig. 2-11 (a), there are no any peaks attributable to impurities and the structure of PBSC is identified as tetragonal, which is in good agreement with the literature result[34]. The as-prepared powder of BZCY exhibits a single perovskite phase structure after calcination at 1100°C for 6h in air. Special attention should be given to the phase reaction between PBSC and BZCY in the catalyst fabrication process and its potential influence on the permeation performance. Mixtures of PBSC and BZCY were heat-treated for 2 h at various temperatures between 900 and 1200°C and the phase composition was analyzed. The results shown in Fig. 2-11 (c, d) reveal that no reaction between PBSC and BZCY occurred at 1200 °C, indicating that the layered perovskite PBSC is chemically compatible with the BZCY membrane.

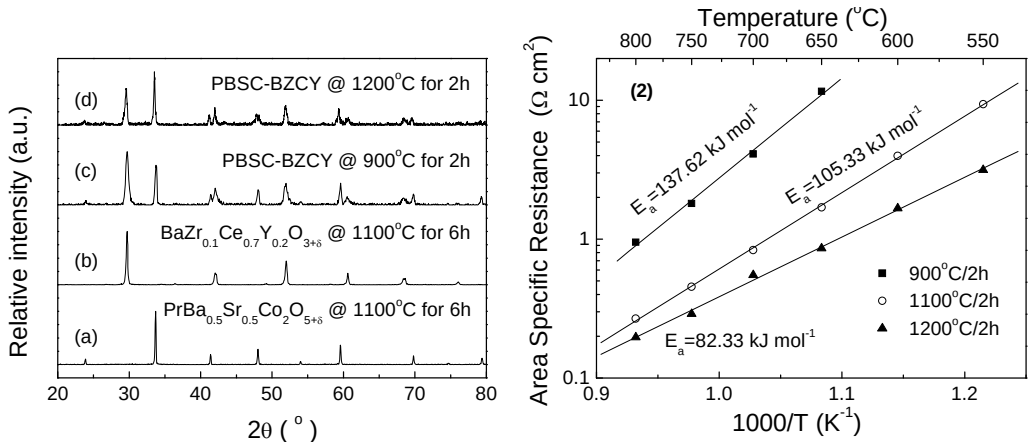

Fig. 2-11 XRD patterns for (a) the pure $Ba_{0.5}Sr_{0.5}Co_2O_{5+\delta}$ (PBSC) powders calcined at 1100°C for 6h, (b) the $BaZr_{0.1}Ce_{0.7}Y_{0.2}O_{3-\delta}$ (BZCY) powders calcined at 1100°C for 6h, and (c, d) PBSC-BZCY composite calcined in air for 2h at 900 and 1100°C, respectively. (2) Area-specific resistance (ASR) results for the symmetrical cells of PBSC-BZCY sintered in air for 2h at 900, 1100 and 1200°C, respectively.

To investigate the effect of sintering temperature on the performances of the PBSC-BZCY composite catalyst, the samples were sintered at 900, 1100 and 1200°C in air for 2h. The ASRs of PBSC-BZCY composite with respect to various sintering temperatures are summarized in Fig. 2-11 (2). From these results, it can be seen that the PBSC-BZCY composite sintered at 1200°C exhibited the lowest ASR values of 0.197Ω cm^2 at 800°C, 0.551Ω cm^2 at 700°C, and 1.669Ω cm^2 at 600°C, which were almost one order of magnitude lower than those of PBSC-BZCY sintered at 900°C for 2h. The apparent activation energies (E_a) of PBSC-BZCY catalyst sintered at different temperatures were also shown in Fig. 2-11 (2). The E_a values of PBSC-BZCY cathodes sintered at 900°C, 1100°C, and 1200°C are 137.62kJ mol^{-1}, 105.33kJ mol^{-1}, and 82.33kJ mol^{-1}, respectively. Low apparent activation energy indicated that PBSC-BZCY composite sintered at 1200°C had less chemical barrier for hydrogen recombination, which resulted in a low ASR value.

One possible origin of the low ASR value of the material sintered at 1200°C is the microstructural enhancement. The fracture cross sections of the PBSC-BZCY composites revealed the microstructure of the optimal sintering temperature (Fig. 2-12). Compared with the composite sintered at 1200°C (Fig. 2-12 (b) and (d)), the PBSC particles sintered at 900°C for 2h (Fig. 2-12 (a)) were smaller. It is well known that a composite cathode can not only reduce the mismatch of thermal expansion between the cathode and the electrolyte, but also minimize the ionic conduction discontinuities in the cathode for solid oxide fuel cells. Employing an elevated sintering temperature can increase the triple-phase-boundary contact of a composite cathode[35]. As shown in Fig. 2-12(c), the composite sintered at 900°C showed relatively poor adhesion at the catalyst/membrane interface and was easily peeled off. Better adhesion was observed when the composite catalysts were sintered at 1200°C (Fig. 2-12 (d)). At 900°C, the temperature was not high enough to result in a structure of sufficient particle necking for good contact and adhesion. At higher temperatures, enhanced necking of the composite electrode particles resulted in improved contact and adhesion. Consequently, the results indicate that a sintering temperature of 1200°C seems to provide a good balance between the conflicting electrode requirements of

maintaining a porous, relatively high surface-area structure while at the same time providing a strong and well-bonded interface with adequate adhesion. It should be noted that the sintering temperature might be further optimized by increasing the sintering temperature to obtain a lower ASR and better interfacial adhesion. However, possible secondary phases might form at elevated temperature between PBSC and BZCY[36].

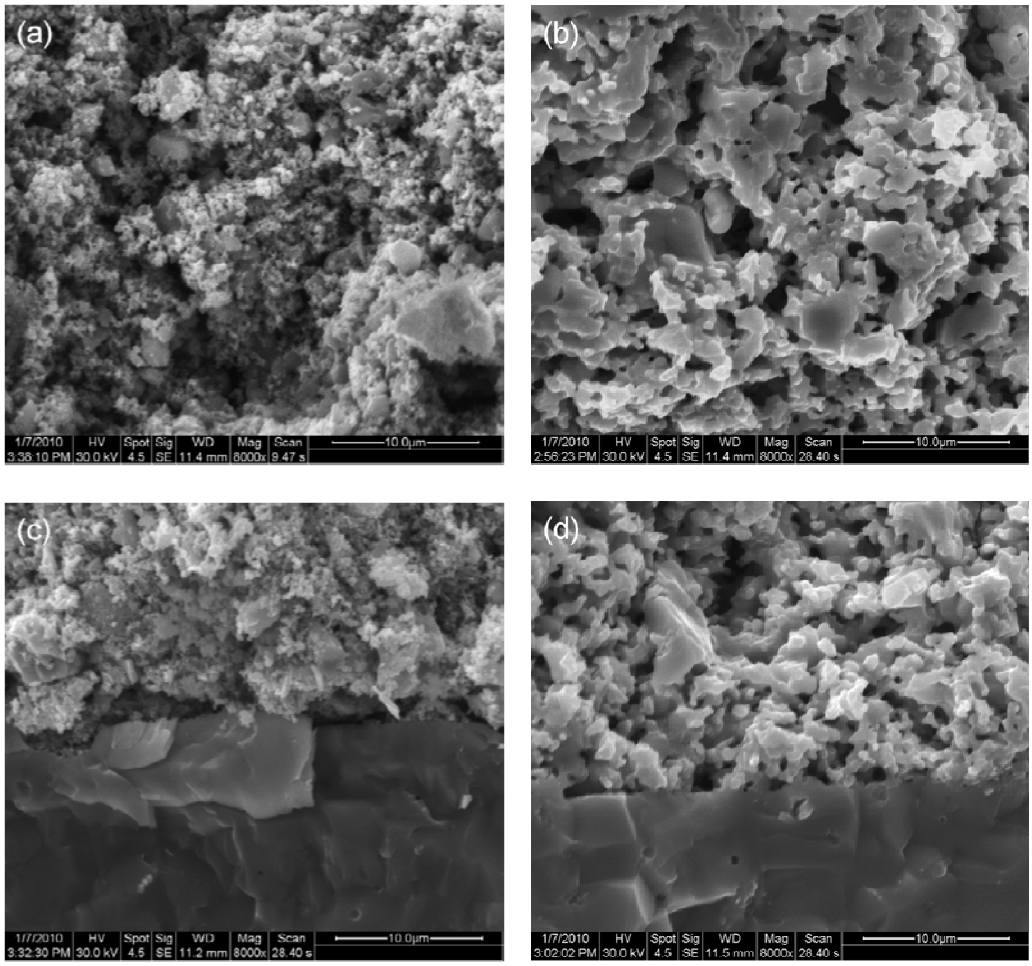

Fig. 2-12 Cross-section images of the post-examined symmetric catalyst. PBSC-BZCY bulk for sintered at 900°C (a) and 1200°C (b) for 2h; (PBSC-BZCY) / (BZCY) interface sintered at 900°C (c) and 1200°C (d) for 2h.

Fig. 2-13 displays the impedance spectra of the membrane measured under open-circuit conditions at different temperatures. The high frequency intercept corresponds to the ohmic resistance (R_o), while the low frequency intercept corresponds to the total resistance (R_t). Therefore, the difference between the high frequency and low frequency intercepts with the real axis represents the total interfacial polarization resistance (R_p), including the catalyst/membrane interfacial resistance and the substrate/membrane interfacial resistance. As expected, the increase of the measuring temperature resulted in a significant reduction of the interfacial polarization resistances as shown in Fig. 2-14 (a), typically from 1.359 Ω cm^2 at 550°C to 0.132 Ω cm^2 at 700°C. The low polarization resistances indicated that PBSC-BZCY composite catalyst was a good candidate for operation at 700°C. As shown in Fig. 2-14 (a), R_t is mainly dominated by R_p

at or below 600°C, however, above 600°C, R_t is mainly dominated by R_o. Further analysis shows that the ratio of R_p to R_t decreases with the increase in operating temperature, from 67% at 550°C to 29% at 700°C, indicating that the membrane performance is significantly limited by R_p at low temperatures. The results confirm that PBSC-BZCY may be a promising catalyst for proton conducting membranes.

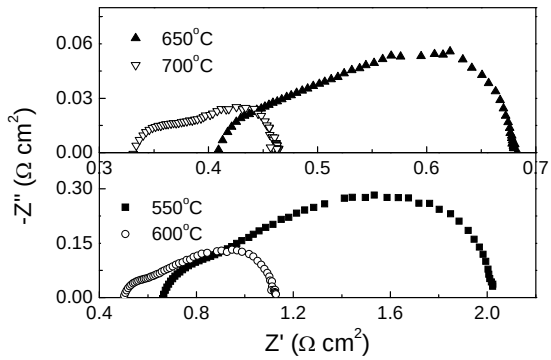

Fig. 2-13 Impedance spectra of the PBSC-BZCY)/(BZCY) membrane measured under open-circuit conditions at different temperatures.

The cross-section micrograph of the modified membrane after the electrochemical tests is provided in Fig. 2-14 (b). As shown in Fig. 2-14 (b), the dense BZCY membrane (ca. 15μm) indicates that the drop-coating technique was successful. Compared with other thin film deposition technologies such as co-pressing, screen-printing and gel-casting, the drop-coating technology is a simple and effective way to obtain a dense membrane. The PBSC-BZCY catalyst has a uniform porous microstructure seen from the picture, resulting in low interfacial polarization resistance and high electrochemical performance.

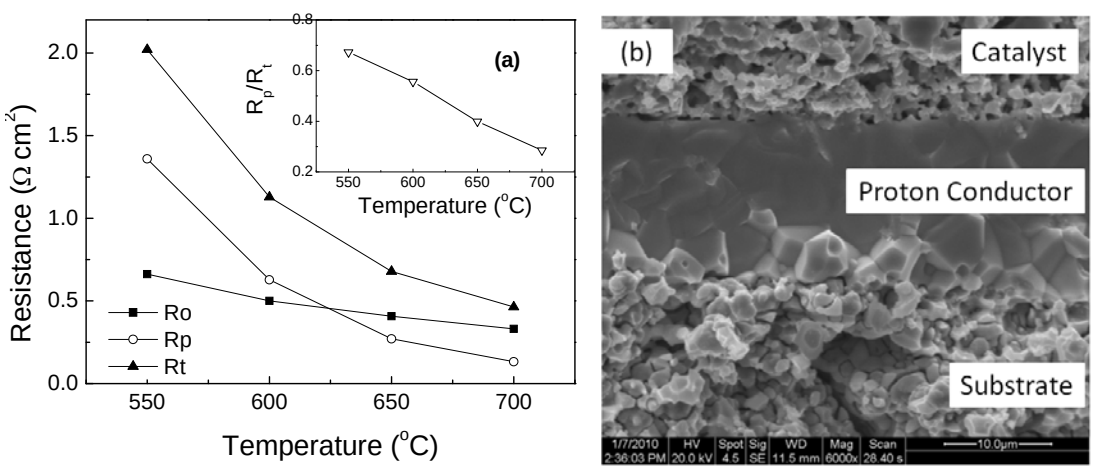

Fig. 2-14 (a) The interfacial polarization resistances (R_p), ohmic resistances (R_o), total resistances (R_t), and the ratio of interfacial polarization resistance to total resistance (R_p/ R_t) obtained from the impedance spectra at different temperatures; (b) Cross-section images of the membrane with catalytic layer and substrate with a 15μm-thick BZCY membrane.

2.5.6 Infiltrated Multiscale porous $Sm_{0.5}Sr_{0.5}CoO_{3-\delta}$-$BaZr_{0.1}Ce_{0.7}Y_{0.2}O_{3-\delta}$ Catalyst for Proton-conducting Hydrogen Separation Membranes

A modified self-assembly approach has recently been developed to synthesize multiscale porous metal oxides[37]. Macropores can be created by using urea as a leavening agent while mesopores inside the shells or walls of the macropores are generated by the self-assembly process[38]. However, it turns out to be very difficult to directly apply such multiscale porous material as cathode in SOFCs and catalyst for hydrogen separation membranes. The main reason is that the multiscale porous material does not possess adequate thermal and mechanical strength to maintain such distinct multiscale porous structure during the typical screen-printing cathode preparation process, which involves grinding or ball-milling cathode powder with a binder to make a cathode ink, screen-printing the cathode ink to an electrolyte surface, and then firing the cathode in a temperature range of 900-1200°C to obtain good contact of the cathode to the electrolyte[39]. To overcome the damage of the multiscale porous cathode structure, infiltration process has been employed in this work to in-situ prepare the multiscale porous cathode. Infiltration method has been frequently used to fabricate nanostructured electrodes, involving adsorption and subsequent decomposition of metal salts at relatively low temperatures[40]. Relatively low fabricating temperature used in the infiltration process is in favor of maintaining the catalytic activity of the cathode and its structural integrity.

In this study, we have developed a multiscale porous composite catalyst of SSC-$BaZr_{0.1}Ce_{0.7}Y_{0.2}O_{3-\delta}$ (BZCY) for proton-conducting separation membranes. The BZCY backbone of the composite cathode is expected to provide continuous pathway for proton conduction while the SSC cathode catalyst coated on the BZCY cathode backbone with disordered multiscale porous structure is expected to exhibit enhanced gas diffusion and enlarged electrochemical reaction sites for hydrogen recombination. The SSC is fabricated in-situ by infiltrating a modified self-assembly precursor, followed by calcinating at 900 ^{o}C for 2h to form multiscale porous structure.

Shown in Fig. 2-15 (a) are the X-ray diffraction patterns of BZCY powder, SSC powder and infiltrated SSC-BZCY composite catalyst. It can be clearly seen that only peaks related to perovskite phase are observed for the BZCY and SSC powders after calcination. No impurity peaks are found for the infiltrated SSC-BZCY composite cathode fired at 900 ^{o}C for 2 h. Fig. 2-15(b) are AC impedance spectra of the membrane under open-circuit conditions. Total cell resistance (R_t), cell ohmic resistance (R_o), and polarization resistance (R_p) were determined from the impedance spectra at different temperatures. As shown in Fig. 2-15(b), the polarization resistances were 0.388, 0.162, and 0.064 $\Omega\cdot cm^2$ at 600, 650 and 700 °C, respectively, which were very low for proton-conducting based materials.

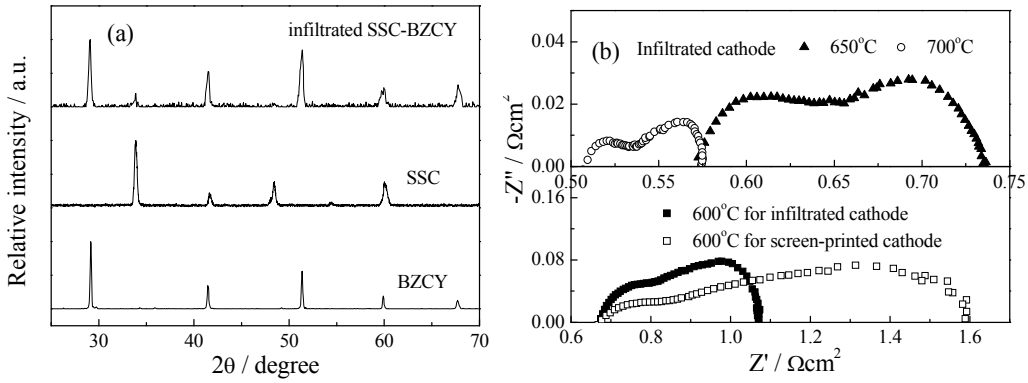

Fig. 2-15 (a) X-ray diffraction patterns of BZCY powder, SSC powder and infiltrated SSC-BZCY composite catalyst. (b) Impedance spectra of the modified membrane measured under open-circuit conditions.

The cross-sectional views of the infiltrated and screen-printed SSC-BZCY composits are shown in Fig. 2-16. Dendritic structure with high porosity are found for the BZCY cathode backbone as shown in Fig. 2-16(a), indicating uninterrupted paths for proton conduction and facile gas transport features favorable for the hydrogen recombination process. After firing the infiltrated precursor, the dendritic BZCY cathode backbones were subsequently coated by SSC catalysts, showing a specific surface area of 1.079 $m^2 \cdot g^{-1}$. The SSC has three-dimensionally open pores with dimensions of hundreds to thousands of nanometers randomly distributed on the BZCY backbone as shown in Fig. 2-16(b). Fig. 2-16(c) shows a screen-printed SSC-BZCY composite catalyst fabricated from the slurry consisting of the SSC and BZCY powders. The SSC powder has similar multiscale microstructure as demonstrated in our previous work[37]. As shown in Fig. 2-16(c), the catalyst reveals a randomly distributed mixture of SSC and BZCY with no visible the multiscale porous SSC structure, probably destroyed during the mechanically mixing process. Fig. 2-16(d) shows a cross-section photograph of the freshly infiltrated composite at high magnification. Macropores produced by a leavening process of urea can be observed in Fig. 2-16(d), and the distribution of these pores is more disordered probably due to the inhomogenous and complicated environment compared with the SSC powder fabricated from precursor solutions in beakers. Small-sized pores and nanoparticles with a size range from 50 to 100 nm generated by the self-assembly process are also found inside the shells or walls of the macropores. Such multiscale porous microstructure and nano-sized particles are expected to significantly enhance catalyst performance due to improved gas diffusion and extended length of TPB sites.

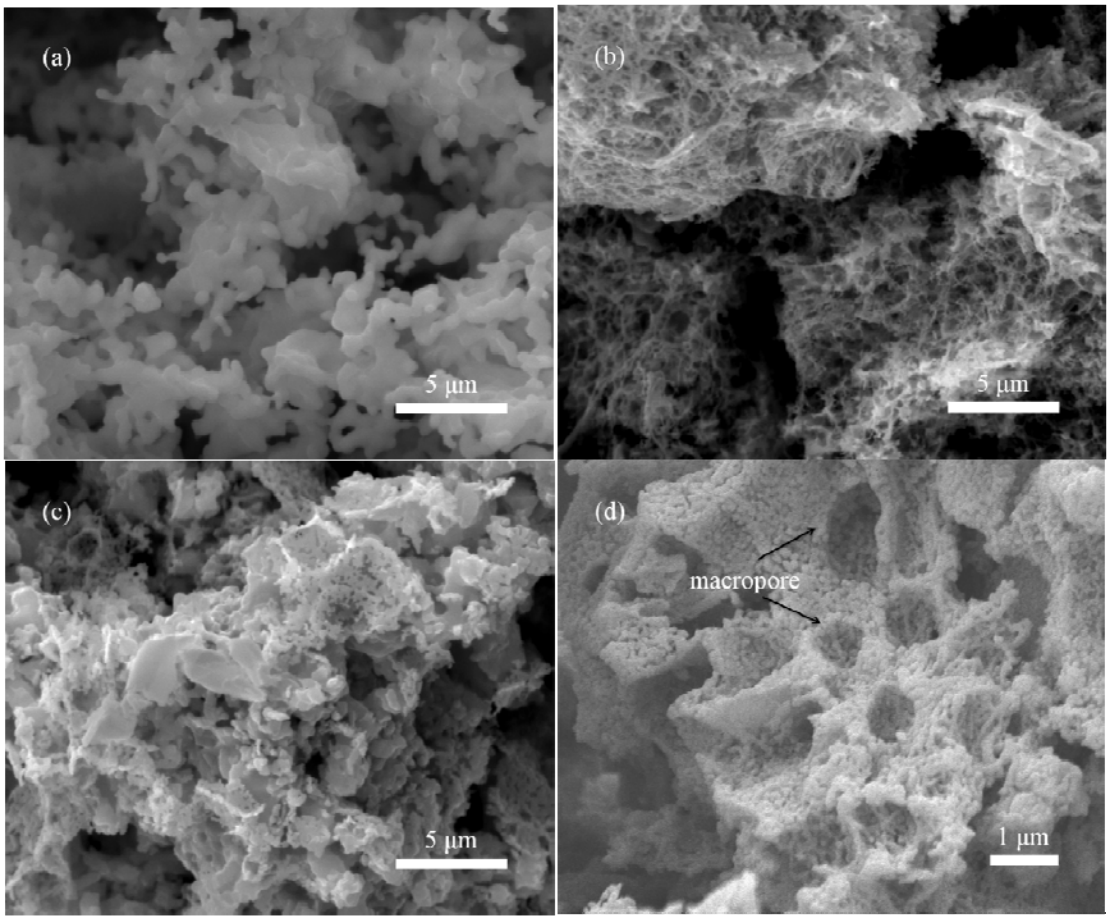

Fig. 2-16 Cross-sectional views for composite catalysts: (a) BZCY electrolyte backbone; (b) infiltrated SSC-BZCY cathode; (c) screen-printed SSC-BZCY cathode; and (d) fresh infiltrated SSC-BZCY cathode at high magnification.

The polarization resistances for different cells with the anode material and similar cathode firing temperature were plotted in Fig. 2-17 (a). At 600 °C, the R_p of infiltrated cathode was much lower than 1.5 Ωcm^2 of a cell based on SSC-BZCY cathode fired at 900 ^oC, while it was still higher than 0.168 Ωcm^2 for the cell with a catalyst firing at 1000 ^oC[62]. The reason for such differences in the measured cell polarization resistances was probably due to the interparticle connectivity. The adhesion of the cathode to the membrane was found to be improved by increasing the firing temperature from 900 to 1000 ^oC. Though the presence of some second phases such as $BaCoO_3$ and $Sm_2Zr_2O_7$ was observed between BZCY and SSC fired at 1000^oC, the cell performance could still be enhanced due to the reduced contact resistance. Consequently, higher cell performance might be achievable by increasing the firing temperature of infiltrated SSC precursor to improve the connectivity between SSC and BZCY backbone. As shown in the experimental section, since the catalyst was coated on the backbone through thermal decomposition process, it was fairly easy to adjust the firing temperature to improve the connectivity between SSC and BZCY backbone. The effect of firing temperature of the infiltrated precursor on the catalyst performance will be systematically evaluated in the future study. At 700^oC, the R_p was comparable to that of the SSC-SDC composite cathode with a cell polarization resistance of 0.066 $\Omega \cdot cm^2$ [41]. Total cell resistances were 1.064, 0.734, and 0.574

$\Omega \cdot cm^2$ at 600, 650 and 700 °C, respectively. The ratio of R_p to R_t decreased with the increase in the operating temperatures, from 36.5% at 600 °C to 11.1% at 700 °C, implying that the cell performance was limited not by the polarization resistance but by the ohmic resistance. Consequently, enhanced cell performance may be expected by using thinner electrolyte film or more conducting electrolyte material with good chemical stability such as BZCY or $BaZr_{0.1}Ce_{0.7}Y_{0.1}Yb_{0.1}O_{3-\delta}$. Further, there was no significant change in the multiscale porous microstructure of the infiltrated catalyst between the tested cell (Fig. 2-17 (b)) and the fresh one (Fig. 2-16(d)).

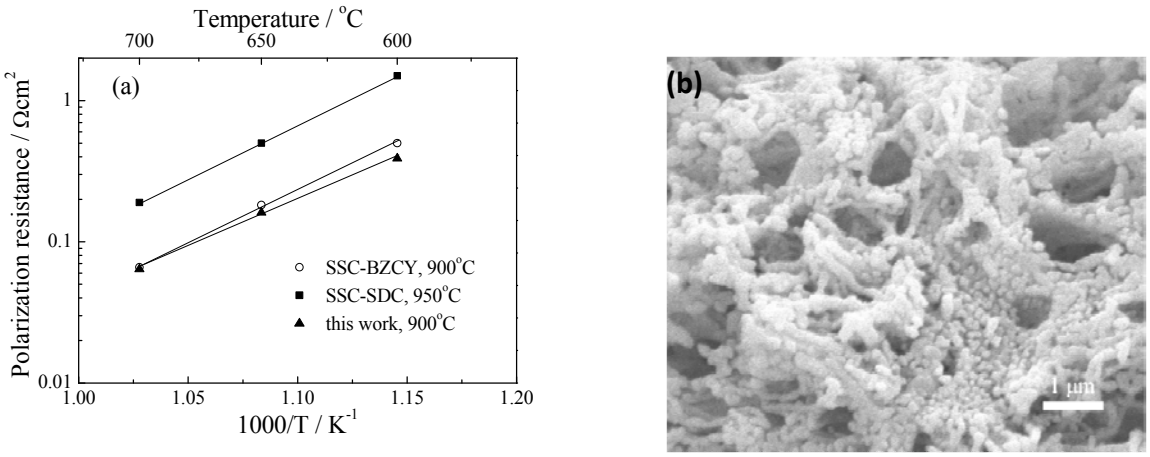

Fig. 2-17 (a) Polarization resistances determined from impedance spectra for cells: Ni-BZCY|BZCY|SSC-BZCY, Ni-BZCY|BZCY|SSC-SDC and Ni-BZCY|BCI|infiltrated SSC-BZCY (this work). (b) Cross-sectional view for short-term durability tested infiltrated SSC-BZCY catalyst at high magnification.

2.5.7 Fabrication and Characterization of Metal/Ceramic-supported Micro-tubular Hydrogen Separation Membrane Based on $BaCe_{0.7}Zr_{0.1}Y_{0.1}Yb_{0.1}O_{3-\delta}$

In the past few years, traditional extrusion techniques have been normally used to fabricate the substrate tubes of the micro-tubular solid oxide fuel cells[42]. Recently, a phase inversion method has been employed to fabricate electrolyte-supported micro-tubular SOFCs with conventional oxygen-ion conducting electrolytes such as yttria-stabilized zirconia (YSZ) and $Ce_{0.8}Sm_{0.2}O_{1.9}$ (SDC). This micro-tubular solid oxide fuel cell design can also be utilized in the hydrogen separation membranes. It has been recently reported that $BaCe_{0.7}Zr_{0.1}Y_{0.1}Yb_{0.1}O_{3-\delta}$ (BCZYYb), a mixed proton and oxide ion conductor, exhibits high proton conductivity[21]. The application of this material with high conductivity is an effective approach for reducing the ohmic loss and cost. In addition, an metal/ceramic support allows a thin membrane to be deposited on the supporting substrate, thus reducing the resistance losses from the contact and yielding improved performance at reduced operating temperatures over an electrolyte-supported cell configuration. Consequently, Ni/BCZYYb-substrate with thin film membrane can be considered as another promising approach to increase the performance of hydrogen separation membrane for operation at reduced atmospheres. In this work, nickel and BCZYYb-supported micro-tubular hydrogen separation membrane based on BCZYYb electrolyte with an outer diameter (O.D.) less than 2 mm was fabricated by phase inversion and dip-coating techniques with a co-firing process.

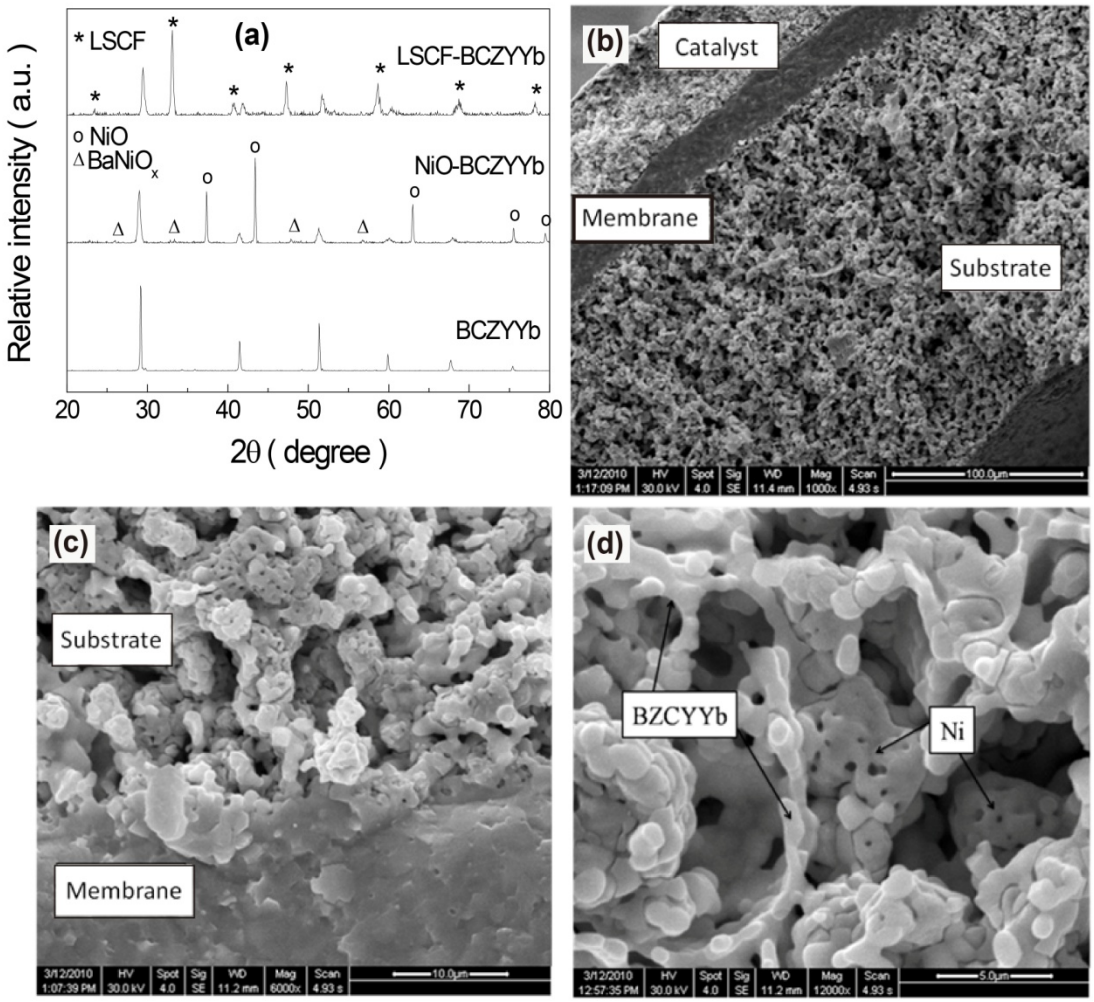

Fig. 2-18 (a) X-ray diffraction patterns of BCZYYb membrane, NiO-BCZYYb substrate and LSCF-BCZYYb catalyst, (b) Cross-section SEM images of a Ø=1.6mm micro-tubular hydrogen separation membrane, (c) the membrane/substrate interface, and (d) porous substrate after tests

As shown in Fig. 2-18 (a), the BCZYYb film after co-sintering with NiO-BCZYYb anode at 1400 ^{o}C for 5 h can be identified as perovskite phase. Some minor peaks corresponding to barium nickel oxide ($BaNiO_x$) are found in the XRD spectrum for the co-sintered NiO-BCZYYb, indicating that trace amount of solid solution between NiO and doped barium cerate might be formed during the high co-sintering process. The XRD peaks of LSCF-BCZYYb catalyst after firing at 1100°C for 2 h are also shown in Fig. 2-18 (a). There are no obvious peaks attributable to impurities, indicating that there are negligible interactions between LSCF and BCZYYb during the catalyst fabrication process. Cross-sectional SEM images of the metal/ceramic-supported micro-tubular cell after testing are presented in Fig. 2-18 (b-d). As shown in Fig. 2-18 (b) the thickness of the substate is about 200 μm and BCZYYb membrane with a thickness of 25 μm was successfully obtained on the substrate tube by dip-coating and co-sintering method. Fig 2-18 (c) reveals that the membrane is dense and free of cracks, adhering very well to the Ni-BCZYYb substrate layer. As shown in Fig. 2-18 (d), uniform porous nickel and BCZYYb

composite substrate microstructures are formed, providing efficient channel for transporting the fuel gas as well as continuous ionic and electronic conducting paths.

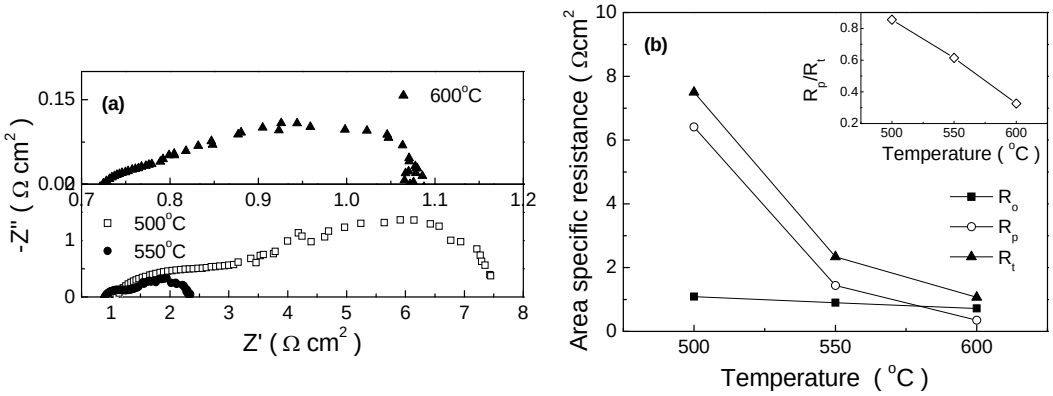

Fig. 2-19 (a) impedance spectra at different temperatures measured under open-circuit conditions, and (b) The total resistance (R_t), interfacial polarization resistance (R_p), and ohmic resistance (R_o) as determined from the impedance spectra as shown in (a). R_p/R_t is also shown in the figure.

Fig. 2-19 displays the impedance spectra of the membrane measured under open-circuit conditions with hydrogen on one side while air on the other side of the membrane at different temperatures. The low frequency intercept corresponds to the total resistance (R_t), including ohmic resistance (R_o) and interfacial polarization resistance (R_p). The difference between the high frequency and low frequency intercepts with the real axis represents the total R_p of the cell, including the catalyst-electrolyte interfacial resistance and the anode-electrolyte interfacial resistance. The ohmic, polarization and total resistances obtained from the impedance spectra are summarized in Fig. 2-19(b). As expected, the increase of the measuring temperature resulted in a significant reduction of the interfacial polarization resistances as shown in Fig. 2-19(b), typically from 6.41 Ωcm^2 at 500 ^oC to 0.35 Ωcm^2 at 600^oC. Further analysis shows that the ratio of R_p to R_t decreases with the increase in the cell operating temperatures, from 85.5 % at 500 ^oC to 32.6 % at 600 ^oC, indicating that the cell performance is significantly limited by R_p at low temperatures. The large R_p value observed in this work implies that electrochemical activity of LSCF catalyst is not sufficient at low temperatures, consistent with previous reports[43]. Therefore, the performances may be improved by using materials with better catalytic performance such as $Ba_{0.5}Sr_{0.5}Co_{0.8}Fe_{0.2}O_{3-\delta}$ (BSCF)[44] and optimizing the electrode microstructure to decrease the electrode polarization.

2.5.8 Permeation Evaluation of $SrCe0._{095}Yb_{0.05}O_3$ Proton Conducting Ceramic and Thin Films

In order to estimate the temperature and isotope effects on permeation, the conductivity of ($SrCe0._{095}Yb_{0.05}O_3$) and ($BaCe_{0.9}Y_{0.1}O_3$) ceramic membranes were examined by AC impedance spectroscopy. Fig. 2-20(a) shows the AC impedance spectra of a $SrCe0._{095}Yb_{0.05}O_3$ sample measured under deuterium (D_2O) and hydrogen (H_2O) conditions at low temperature where separate grain and grain boundary contributions are evident. Extrapolation of the grain boundary and bulk contributions to higher temperature where AC impedance can typically only distinguish total conductivity was used to construct the plot in Fig. 2-20(b) displaying the separate grain, grain boundary and total conductivity versus temperature for $SrCe0._{095}Yb_{0.05}O_3$ under H_2O-Ar

atmosphere. Fig. 2-21 displays the conductivity versus reciprocal temperature (1/T) for $SrCe0._{095}Yb_{0.05}O_3$ charged with deuterium (D_2O-Ar) versus hydrogen (H_2O-Ar). The measured grain boundary and total conductivity in temperature range where accessible are displayed.

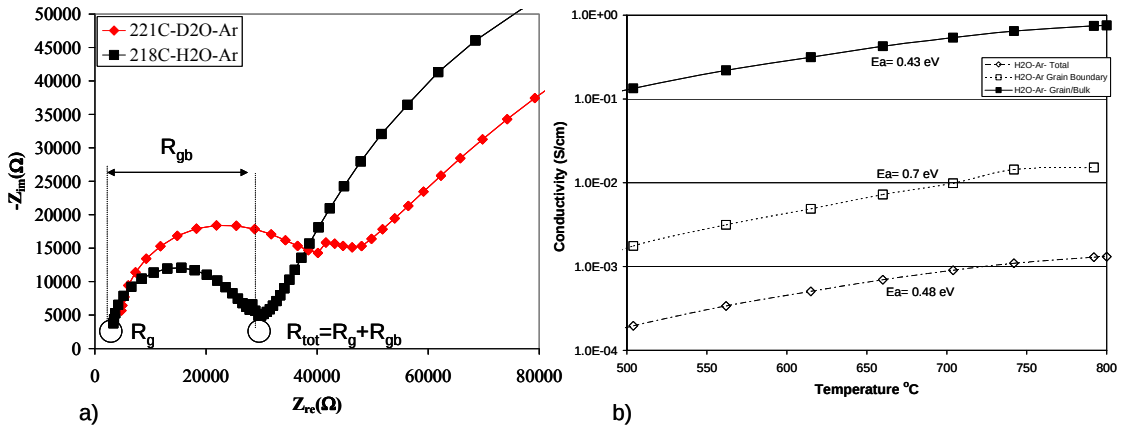

Fig. 2-20 $SrCe0._{095}Yb_{0.05}O_3$ (a) AC impedance spectra and (b) separate conductivity (S/cm) versus temperature (^oC) contributions under hydrogen atmosphere (Ar-H_2O).

Table 2-2 Activation Energy (eV) of Conductivity in D_2 and H_2 charged $SrCe_{0.95}Yb_{0.05}O_3$ samples.

Contribution to Conductivity	***H_2O-Ar***	***D_2O-Ar***
	Ea (eV)	Ea (eV)
Total	0.48	0.44
Grain/bulk	0.43	-
Grain Boundary	0.7	0.68

Table 2-2 summarizes the activation energy of different contributions to conductivity for hydrogen and deuterium charged samples of $SrCe0._{095}Yb_{0.05}O_3$. The grain boundary contribution is seen to have a significantly higher activation energy near 0.7 eV as compared with bulk and total conductivity near ~0.4-0.5 eV. This level of activation energy corresponds well with literature studies of proton conduction of barium cerate[45] and bariuim zirconate materials[46].

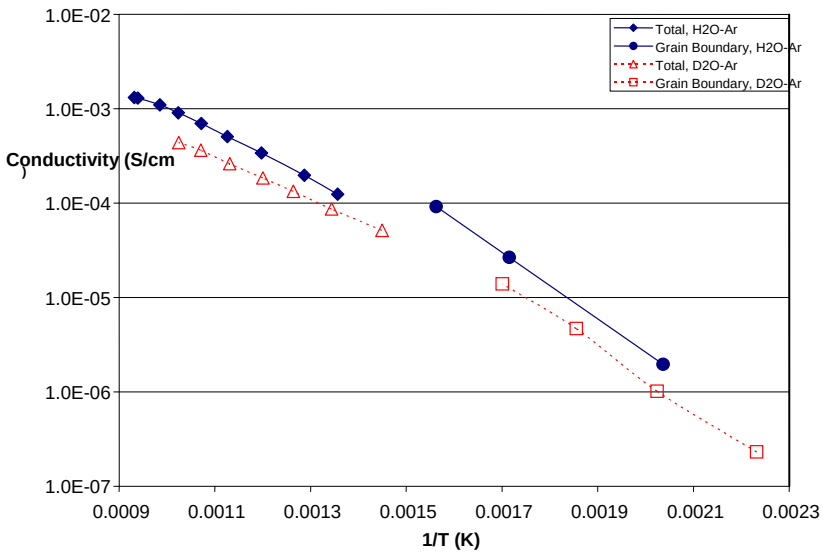

Figure 2-21 Hydrogen versus deuterium conductivity (S/cm) as function of reciprocal temperature (1/T) for $SrCe0._{095}Yb_{0.05}O_3$

It is also seen that the conductivity of deuterium is lower than the proton conductivity due to the larger mass being transported via hopping through He oxygen sublattice. At 700°C total conductivity of 4.4 X 10^{-3} S/cm for deuterium as compared to 9.0 X 10^{-3} S/cm for protons. Tritium conductivity is expected to be correspondingly lower than deuterium necessitating longer times and/or larger membrane area for removal from He gas streams. Total energy dose rates from tritium decay have been estimated to be 5.7 X 10^{15} eV/(s cm^3) in proton ceramics. TEM dose calculations have shown this will be achieved in seconds to minutes of high resolution TEM exposure- no radiation induced damage was initial observed and will not be expected. However, during long term membrane use, some of the tritium attached to oxygen sublattice inside the perovskite structure may be "trapped". Decay of tritium to He^3 can result in trapped helium gas "bubbles" that may lead to fracture and failure of the ceramic membrane. Therefore, while not true radiation damage from emitted beta particle, damage of this type should be investigated by further mechanical property evaluation.

3. CONCLUSIONS

Several types of high temperature proton conductors have been systematically investigated in this project for tritium separation in NGNP applications. One obstacle for the field application is the chemical stability issues in the presence of steam and CO_2 for these proton conductors. Several strategies to overcome such issues have been evaluated, including A site doping and B site co-doping method for perovskite structured proton conductors. Novel zirconium free proton conductors have also been developed with improved electrical conductivity and enhanced chemical stability. Novel catalytic materials for the proton conducting separation membranes have been investigated. A tubular geometry proton conducting membrane has been developed for the proton separation membranes. Total dose rate estimated from tritium decay (beta emission) under realistic membrane operating conditions, combined with electron irradiation experiments indicate that proton ceramic materials possess the appropriate radiation stability for this application. Although significant progress and extensive knowledge have been achieved in this study, further exploration on novel high temperature proton conductors with high proton conductivity and enhanced chemical stability are still urgently needed for effective tritium sequestration in high temperature nuclear energy systems.

NEUP-09-510 PUBLICATION AND PRESENTATION LIST

Journal Publications

1. S. Wang, F. Zhao, L. Zhang and F. Chen, "Synthesis of $BaCe_{0.7}Zr_{0.1}Y_{0.1}Yb_{0.1}O_{3-\delta}$ proton conducting ceramic by a modified Pechini method", *Solid State Ionics* In press. Doi: 10.1016/j.ssi.2011.05.014
2. F. Zhao, Q. Liu, S. Wang and F. Chen, "Infiltrated multiscale porous cathode for proton-conducting solid oxide fuel cells" *Journal of Power Sources*, 196 (2011) 8544–8548.
3. F. Zhao, S. Wang, L. Dixon and F. Chen, "Novel $BaCe_{0.7}In_{0.2}Yb_{0.1}O_{3-\delta}$ proton conductor as electrolyte for intermediate temperature solid oxide fuel cells", *Journal of Power Sources*, 196 (2011) 7500-7504.
4. F. Zhao, C. Jin, C. Yang, S. Wang and F. Chen, "Fabrication and characterization of anode-supported micro-tubular SOFC based on $BaZr_{0.1}Ce_{0.7}Y_{0.1}Yb_{0.1}O_{3-\delta}$ electrolyte", *Journal of Power Sources*, 196 (2011) 688-691.
5. S. Wang, F. Zhao, L. Zhang, K. Brinkman and F. Chen, "Stability and electrical property of $Ba_{1-x}Sr_xCe_{0.8}Y_{0.2}O_{3-\delta}$ high temperature proton conductor", *Journal of Alloys and Compounds*, 506 (2010) 263-267.
6. F. Zhao and F. Chen, "Performance of solid oxide fuel cells based on proton-conducting $BaCe_{0.7}In_{0.3-x}Y_xO_3$ electrolyte", *International Journal of Hydrogen Energy*, 35 (2010) 11194-11199.
7. F. Zhao, S. Wang, K. Brinkman and F. Chen, "Layered perovskite $PrBa_{0.5}Sr_{0.5}Co_2O_{5+\delta}$ as high performance cathode for solid oxide fuel cells using proton conducting electrolyte", *Journal of Power Sources*, 195 (2010) 5468-5473.
8. F. Zhao, Q. Liu, S. Wang, K. Brinkman and F. Chen, "Synthesis and characterization of $BaIn_{0.3-x}Y_xCe_{0.7}O_{3-\delta}$ (x=0, 0.1, 0.2, 0.3) proton conductors", *International Journal of Hydrogen Energy*, 35 (2010) 4258-4263.
9. K. Brinkman, E. B. Fox, P. Korinko, B. Lascola and F. Chen, "Structure/property relations in bulk versus solution derived proton conducting ceramics of the form $SrCe_{0.95}Yb_{0.05}O_{3-\delta}$ with applications in membrane separations", in Proceedings of Functional Oxide Nanostructures and Heterostructures, Materials Research Society (MRS) Spring Meeting, San Francisco CA, April 5-9, 2010.

Patent Applications

K. Brinkman, P. Korinko, E. Fox and F. Chen, "Proton Conducting Ceramics in Membrane Separations", US Patent Application, 13/066,166, 2011.

Conference Presentations

1. S. Wang, S. Fang, F. Zhao, K. Brinkman, and F. Chen, "Synthesis and Electrical Properties of Ultrafine Grained $BaCeO_3$ Based Proton Conductors", in the Nanotechnology General Session, in the 220th Electrochemical Society Meeting & Electrochemical Energy Summit in Boston, MA, October 9-14, 2011.

2. K. Brinkman, R. Lascola, F. Chen, S.G. Kang and D. Sholl, "Structure/Property Relations in Spark Plasma versus Conventionally Sintered Proton conducting Ceramics of the Form SrCe0.95Yb0.05O3-δ with Applications in Membrane Separations", The International Chemical Congress of Pacific Basin Societies, Honolulu, Hawaii, December 15-20, 2010.

3. F. Zhao and F. Chen, "Performance of SOFC with Proton-Conductor $BaCe_{0.7}In_{0.2}Yb_{0.1}O_3$ Electrolyte", The 15th Solid State Proton Conductors conference, Santa Barbara, CA, August 15-20, 2010.
4. S. Wang and F. Chen, "Synthesis and Characterization of $BaCe_{0.7}Zr_{0.1}Y_{0.1}Yb_{0.1}O_{3-\delta}$ Proton Conducting Ceramic", The 15th Solid State Proton Conductors conference, Santa Barbara, CA, August 15-20, 2010.
5. F. Zhao and F. Chen, "Fabrication and Characterization of $BaIn_{0.3-x}Y_xCe_{0.7}O_{3-\delta}$ Proton Conductor", The 7th Symposium on Ionic and Mixed Conducting Ceramics, The 217th Electrochemical Society Meeting, Vancouver, Canada, April 25-30, 2010.
6. K. Brinkman and F. Chen, "Structure/Property Relations in Bulk Versus Solution Derived Proton Conducting Ceramics of the Form $SrCe_{0.95}Yb_{0.05}O_{3-\delta}$ with Applications in Membrane Separations", Symposium N: Functional Oxide Nanostructures and Heterostructures, Materials Research Society (MRS) Spring Meeting, San Francisco CA, April 5-9, 2010

REFERENCES

[1] Sherman S., "Nuclear reactor/hydrogen process interface", Department of Energy Hydrogen Program Annual Merit Review Proceedings, May 15–18, 2007, Washington, D.C.

[2] Medeiros R.B., Godhino R.O., Mattos M., "Comparison of the efficacy of biodegradable and non-biodegradable scintillation liquids on the counting of tritium- and [C-14]-labeled compounds", Brazilian Journal of Medical and Biological Research, 2003, 36, 1733.

[3] Ohashi H., Sherman S.R., "Tritium movement and accumulation in the NGNP system interface and hydrogen plant", INL/EXT-07-12746, Idaho National Laboratory, June 2007.

[4] Sherman S.R., Adams T.M., "Tritium barrier materials and separation systems for the NGNP", WSRC-STI-2008-00358, Savannah River National Laboratory, August 2008.

[5] Glasbrenner H., Klewe-Nebenius H., Bruns M., Pfennig G., Penzhorn R.D., Ache H.J., "Surface analytical investigation of the tritium getter ZrCo after exposure to various gases", Mikrochimica Acta, 1992, 107, 207.

[6] Wang W., Long X., Cheng G., Peng S., Yang B., "Tritium absorption-desorption characteristics of $LaNi_{4.25}Al_{0.75}$", Journal of Alloys and Compounds, 2007, 441, 359.

[7] Penzhorn R.D., Devillers M., Sirch M., "Evaluation of ZrCo and other getters for tritium handling and storage", Journal of Nuclear Materials, 1990, 170, 217.

[8] Peachy N.N., Snow R.C., Dye R.C., "Composite Pd/Ta metal membranes for hydrogen separation", Journal of Membrane Science, 1996, 111, 123.

[9] Hou K., Hughes R., "The effect of external mass transfer, competitive adsorption and coking on hydrogen permeation through Pd/Ag membranes", Journal of Membrane Science, 2002, 206, 119.

[10] Dorris S.E., Lee T.H., Balachandran U., "Metal/ceramic composites with high hydrogen permeability", US Patent, 6,569,226, May 27, 2003.

[11] Iwahara H., Esaka T., Uchida H., Maeda N., "Proton conduction in sintered oxides and its application to steam electrolysis for hydrogen production", Solid State Ionics, 1981, 3-4, 359.

[12] Bonnett I., Busigin A., Shapiro A., "Tritium removal and separation technology developments", Fusion Science and Technology, 2008, 54, 209.

[13] Tanaka M., Katahira K., Asakur Y., Uda T., Iwahara, H., Yamamoto I., "Hydrogen extraction using one-end closed tube made of $CaZrO_3$-based proton-conducting ceramic for tritium recovery system", Journal of Nuclear Science and Technology, 2004, 41, 61.

[14] Haile S.M., Staneff G, Ryu K.H., "Non-stoichiometry, grain boundary transport and chemical stability of proton conducting perovskites", Journal of Materials Science, 2001, 36, 1149.

[15] Yang L., Wang S., Kevin B., Liu M.F., Ze L., Zhe C., Liu M., "Enhanced sulfur and coking tolerance of a mixed ion conductor for SOFCs: $BaZr_{0.1}Ce_{0.7}Y_{0.2-x}Yb_xO_{3-\delta}$", Science, 2009, 326, 126.

[16] Chen F., Søensen O.T., Meng G., Peng D., "Preparation of Nd-doped barium cerate through different routes", Solid State Ionics, 1997, 100, 63.

[17] Fabbri E., D'Epifanio A., Bartolomeo E. D., Licoccia S., Traversa E., "Tailoring the chemical stability of $Ba(Ce_{0.8-x}Zr_x)Y_{0.2}O_{3-\delta}$ protonic conductors for intermediate temperature solid oxide fuel cells (IT-SOFCs)", Solid State Ionics, 2008, 179, 558.

[18] Fjeld H., Kepaptsoglou D.M., Haugsrud R., Norby T., "Charge carriers in grain boundaries of 0.5% Sr-doped $LaNbO_4$", Solid State Ionics, 2009, 181, 104.

[19] Zuo C., Zha S., Liu M., Hatano M., Uchiyama M., "$Ba(Zr_{0.1}Ce_{0.7}Y_{0.2})O_{3-\delta}$ as an electrolyte for low-temperature solid-oxide fuel cells", Advanced Materials, 2006, 18, 3318.

[20] Barison S., Battagliarin M., Cavallin T., Doubova L., Fabrizio M., Mortalo C., Boldrini S., Malavasi L., Gerbasi R., "High conductivity and chemical stability of $BaCe_{1-x-y}Zr_xY_yO_{3-\delta}$ proton conductors prepared by a sol-gel method", Journal of Materials Chemistry , 2008, 18, 5120.

[21] Bi L., Zhang S.Q., Zhang L., Tao Z.T., Wang H.Q., Liu W., "Indium as an ideal functional dopant for a proton-conducting solid oxide fuel cell", International Journal of Hydrogen Energy, 2009, 34, 2421.

[22] Matsumoto H., Kawasaki Y., Ito N., Enoki M., Ishihara T., "Relation between electrical conductivity and chemical stability of $BaCeO_3$-based proton conductors with different trivalent dopants", Electrochemical and Solid-State Letters, 2007, 10, B77.

[23] Bi L., Zhang S.Q., Fang S.M., Tao Z.T., Peng R.R., Liu W., "A novel anode supported $BaCe_{0.7}Ta_{0.1}Y_{0.2}O_{3-\delta}$ electrolyte membrane for proton-conducting dolid oxide fuel cell", Electrochemistry Communications, 2008, 10, 1598.

[24] Giannici F., Longo A., Balerna A., Kreuer K.D., Martorana A., "Indium doping in barium cerate: The relation between local symmetry and formation and mobility of protonic defects", Chemistry of Materials, 2007, 19, 5714.

[25] Ding D., Li L., Feng K., Liu Z., Xia C., "High performance Ni–Sm_2O_3 cermet anodes for intermediate-temperature solid oxide fuel cells", Journal of Power Sources, 2009, 187, 400.

[26] Shimura T., Tanaka H., Matsumoto H., Yogo T., "Influence of the transition-metal doping on conductivity of a $BaCeO_3$-based protonic conductor", Solid State Ionics, 2005, 176, 2945.

[27] Gorbova E., Maragou V., Medvedev D., Demin A., Tsiakaras P., "Investigation of the protonic conduction in Sm doped $BaCeO_3$" Journal of Power Sources, 2008, 182, 207.

[28] Zhao F., Liu Q., Wang S.W., Brinkman K., Chen F., "Synthesis and characterization of $BaIn_{0.3-x}Y_xCe_{0.7}O_{3-\delta}$ (x=0, 0.1, 0.2, 0.3) proton conductors", Internal Journal of Hydrogen Energy, 2010, 35, 4258.

[29] Osman N., Talib I., Hamid H., Jani A., "Characterization, electrical conduction and stability of Yb-doped barium cerate prepared by sol-gel method", Ionics, 2008, 14, 407.

[30] Katahira K., Kohchi Y., Shimura T., Iwahara H., "Protonic conduction in Zr-substituted $BaCeO_3$", Solid State Ionics, 2000, 138, 91.

[31] Adler S.B., "Factors governing oxygen reduction in solid oxide fuel cell cathodes", Chemical Reviews, 2004, 104, 4791.

[32] Zhang K., Ge L., Ran R., Shao Z.P., Liu S.M., "Synthesis, characterization and evaluation of cation-ordered $LnBaCo_2O_{5+\delta}$ as materials of oxygen permeation membranes and cathodes of SOFCs", Acta Materialia, 2008, 56, 4876.

[33] Chen D.J., Ran R., Zhang K., Wang J., Shao Z.P., "Intermediate-temperature electrochemical performance of a polycrystalline $PrBaCo_2O_{5+\delta}$ cathode on samarium-doped ceria electrolyte", Journal of Power Sources, 2009, 188, 96.

[34] Zhu C.J., Liu X.M., Yi C.S., Yan D.T., Su W.H., "Electrochemical performance of $PrBaCo_2O_{5+\delta}$ layered perovskite as an intermediate-temperature solid oxide fuel cell cathode", Journal of Power Sources, 2008, 185, 193.

[35] Fukunaga H., Ihara M., Sakaki K., Yamada K., "The relationship between overpotential and the three phase boundary length", Solid State Ionics, 1996, 86-88, 1179.

[36] Tolchard J.R., Grande T., "Chemical compatibility of candidate oxide cathodes for $BaZrO_3$ electrolytes", Solid State Ionics, 2007, 178, 593.

[37] Liu Q., Zhao F., Dong X., Yang C., Chen F., "Synthesis and application of porous $Sm_{0.2}Ce_{0.8}O_{1.9}$ nanocrystal aggregates", Journal of Physical Chemistry C, 2009, 113, 17262.

[38] Whitesides G., Mathias J., Seto C., "Molecular self-assembly and nanochemistry-a chemical strategy for the synthesis of nanostructures", Science, 1991, 254, 1312.

[39] Piao J., Sun K., Zhang N., Xu S., "A study of process parameters of LSM and LSM-YSZ composite cathode films prepared by screen-printing", Journal of Power Sources, 2008, 175, 288.

[40] Sholklapper T., Kurokawa H., Jacobson C., Visco S., Jonghe L., "Nanostructured solid oxide fuel cell electrodes", Nano Letters, 2007, 7, 2136.

[41] Sun W., Yan L., Lin B., Zhang S., Liu W., "Symmetric redox supercapacitor based on micro-fabrication with three-dimensional polypyrrole electrodes", Journal of Power Sources, 2010, 195, 3155.

[42] Suzuki T., Funahashi Y., Yamaguchi T., Fujishiro Y., Awano M., "Fabrication and characterization of micro tubular SOFCs for advanced ceramic reactors", Journal of Alloys and Compounds, 2008, 451, 632.

[43] Kuhn J., P Matter., Millet J., Watson R., Ozkan U., "Oxygen exchange kinetics over Sr- and Co-doped $LaFeO_3$", Journal of Physical Chemistry C, 2008, 112, 12468.

[44] Shao Z.P., Haile S.M., "A high-performance cathode for the next generation of solid-oxide fuel cells", Nature, 2004, 431, 170.

[45] Haile S.M., West D.L., Campbel J., "The role of microstructure and processing on the proton conducting properties of gadolinium-doped barium cerate", Journal of Materials Research, 1998, 13, 1576.

[46] Babilo P., Uda T., Haile S.M., "Processing of yttrium-doped barium zirconate for high proton conductivity", Journal of Materials Research, 2007, 22, 1322.